

Parameters of the Graciosa telescope
and
The dust distribution in spiral galaxies

Annemieke Janssen
Supervisor: R.F. Peletier

December 8, 2009

Abstract

This report contains two parts: an instrumental part about the Gratama telescope in Groningen, and a part about the dust distribution in 23 spiral galaxies. The first part describes how some parameters of the telescope were determined. It involves the pixel size of about $0.56''/\text{pixel}$, the linearity which has deviations up to 0.2% and the illumination correction.

In the second part is described how the dust distribution was obtained in 23 spiral galaxies observed with the Sloan Digital Sky Survey (SDSS). These are both bright and faint galaxies of morphological type T2, T3, T4 and T5. The galaxies were separated in arms and interarm regions to find out whether the arms contain more dust. Elliptical isophotes were fitted to the galaxies in the g and z band and gave the light intensity profile in the total galaxy, the arms and the interarms. From this, the scale length ratio $\frac{h_g}{h_z}$ has been computed for all parts of the galaxy. The scale length ratio is a good measure for the amount of dust, and the following conclusions were drawn: The later type galaxies contain more dust than the early types, which is expected [14]. There is also a significant difference between the arms and interarms; the arms contain more dust than the interarms which is expected as well [9]. Finally it is discussed what should be done to express the scale length ratios in optical depth. A model from Beckman et al. [9] can be used but with scale lengths in only two bands it is difficult to give reliable values.

Contents

1	Introduction	2
2	Parameters of the telescope	3
2.1	Introduction	3
2.2	Gratama Telescope	3
2.3	Pixel size	3
2.3.1	Theory	3
2.3.2	Practice	4
2.4	Linearity	4
2.4.1	Theory	4
2.4.2	Practice	4
2.5	Illumination correction	6
2.5.1	Theory	6
2.5.2	Practice	8
3	Distribution of dust in spiral galaxies	11
3.1	Introduction	11
3.2	Data	12
3.3	Making masks	12
3.4	Scale lengths	16
3.5	The model	16
3.6	Results	17
3.6.1	Metallicity	19
3.6.2	Sample discussion	19
3.7	Conclusion	19
A	Data Gratama telescope	24
B	STL-6303E Typical Specifications	25
C	Galaxies	26
D	Least squares fits: tables	31
E	Least squares fits: plots	35

Chapter 1

Introduction

The opening of the Gratama telescope was a starting point for combining practical work with fundamental research of spiral galaxies. Because many parameters of the new telescope in Groningen are not known yet, I determined some of them, namely the pixel size and the linearity. Measurements have been done to determine the illumination correction, but because the mirrors of the telescope moved, the results are no longer reliable.

Once the most important parameters of the telescope were known, it was possible to study the galaxies of interest. However, because of bad weather the Gratama telescope was not used for observing galaxies, the data comes from the SDSS survey instead. Spirals of different morphological types (Type 2,3,4 and 5) and absolute magnitudes were used to find out how the dust in these spirals is distributed: mainly in the arms or in the interarm regions? A pilot study on three galaxies by Beckman et al. showed that probably most dust is found in the arms [9]. Their method will be used here to more galaxies; 23 in total.

Galactic dust absorbs and scatters blue light much more than red light, so images in both filters were compared with each other. If the stellar and dust distribution are assumed to be radially exponential, more blue than red light will be absorbed near the centre of the galaxy. This makes the scale length in the blue longer than in the red. The ratio between these two scale lengths is an indication of the amount of dust in the galaxy. To be able to say something explicit about the amount of dust and its distribution, models were made (by Disney et al [22]) to match the observed results as well as possible. From these, new models were developed in which parameters, like the amount of scattering and the geometry of the dust, can be varied. Because the difference between arms and interarms has to be studied, these regions should first be separated from each other. The scale length ratios in both regions can then be compared.

Chapter 2

Parameters of the telescope

2.1 Introduction

The Gratama telescope is located on top of the Bernoulliborg, Zernikelaan in Groningen, The Netherlands. This telescope is quite new and was opened at 11 September 2008. When a new telescope starts operating, some tests have to be done with the telescope and the CCD to see how they work in practice. The dates at which these tests were done are given in Appendix A, so the results can be reproduced or the data from the telescope archive can be used for other tests. During the first operational year of the telescope many changes have been applied to the telescope, so not all results can be applied to current-day data. This is the case with the illumination correction. The results of the CCD tests are expected to be still correct, these are the pixel size in arc seconds and the linearity. This chapter includes the methods used to find these results, and how these results compare with other telescopes.

2.2 Gratama Telescope

The Gratama telescope is a two mirror Ritchey-Chrétien telescope [4], so the two mirrors are hyperbolic. Furthermore the aperture of the first mirror has a diameter of 40 cm. All tests have been done with a CCD attached to the telescope, which is a STL-6303E CCD from the producer SBIG. For specifications, see appendix B.

2.3 Pixel size

2.3.1 Theory

One of the parameters of the telescope that had to be determined was the pixel size of the CCD in arc seconds. The pixel size is already known in microns (9 by 9 micron), but not in arc seconds. One might want to know the spatial separation of two objects on the CCD, and the accuracy in this. Stars in the Landolt standard field SA113 [2] have been observed. First the pixel locations of different stars on the CCD were determined, and then the right ascension α in hours and declination δ in degrees were looked up in SIMBAD. SIMBAD got the co-ordinates from the '2Mass all sky catalogue of point sources' which gives them accurate to at least tens of arc seconds.

To get the right position of the stars on the CCD, a Gaussian has been fit to them using `imexamine` in IRAF. The x and y co-ordinates of the top accurately give the position of the star. Since the separations of all stars are known in pixels as well as in arc seconds, the pixel size can be given in "/pixel. Note that we assume the pixels to be perfect squares and do not bother about x or y directions.

name	Rx	Ry	Bx	By	Vx	Vy	α	δ
195	242.2	193.4	266.0	195.2	239.08	192.33	21:43:40.80	+00 17 23.3
158	2303.7	704.8	2327.2	706.3	2300.69	703.14	21:42:21.78	+00 14 10.2
191	421.5	363.3	445.4	364.9	418.17	361.75	21:43:33.57	+00 15 55.8
156	2287.4	915.8	2310.8	917.0	2284.1	914.22	21:42:21.715	+00 12 09.98
153	2653.3	636.2	2676.6	637.8	2650	634.85	21:42:08.88	+00 15 05.5
307	522.6	141.2	546.8	143.1	519.14	140.49	21:43:30.42	+00 18 04.9
177	1389.4	569.2	1412.9	570.3	1386.46	567.77	21:42:56.53	+00 14.44.4

Table 2.1: The stars from the standard field SA113, used for determining the pixel size.

2.3.2 Practice

The first observations produced the data for determining the pixel size. These are exposures in the B,V and R filter. For the data reduction a dark frame of two seconds functions as bias frame. A bias subtracted darkframe with the right exposure time has been subtracted as well. Because we did not yet know the option of making a 'real' darkframe a normal exposure through the H-alpha filter was taken (which lets very little light pass and is in practice almost a darkframe). The result has been divided by a flat field. Because the flats in the R filter contained stars already these could not be used, so the flat field in the V filter has been used to flat field the R exposures. Because the illumination pattern in the V and R filter do not differ much this should not be a problem.

Finally all possible combinations of the stars 158, 195, 156, 191,153,177 and 307 were used (see table 2.1). This was done in the B,V and R filter. Of all these computed values for the pixel size the mean and standarddeviation were taken. The results are: 0.5654 ± 0.0009 "/pixel in the R filter, 0.566 ± 0.001 "/pixel in the B filter and 0.5656 ± 0.0006 "/pixel in the V filter. The pixel size has been determined separately in the three filters, and the differences are shown to be small. The only deflecting part in the telescope, which causes different images at different wave lengths, is the filter itself which is made by glass. Another parametre that might affect the pixel size is the temperature of the CCD, this was $-5^{\circ}C$ during the observations.

2.4 Linearity

2.4.1 Theory

A CCD should respond as linearly as possible to the incoming light. In general CCD's are quite linear in the middle of their range. But for just a few counts or at levels close to saturation, they are expected to become less linear. For a few counts the noise will become important, and if a pixel is almost saturated, the chance to catch a photon becomes smaller. Both influence the linearity. Especially when doing photometry it is very important to know the linearity of the CCD. The linearity test was done with flat fields of different integration times. The longer the integration time, the more counts are expected to be measured. There were already sky flats available from the gain test but these were not useful since the sky got darker during and between the exposures.

2.4.2 Practice

For the determination of the linearity, dome flats have been used. The dome flats were made in daytime with closed dome and the fluorescent light switched on. This gives a constant illumination of the CCD. Integration times were doubled until the pixels were saturated and then halved again to check that the illumination had been constant during the test. This gave exposure times of: 1, 2, 4, 8, 16, 20, 22 seconds.

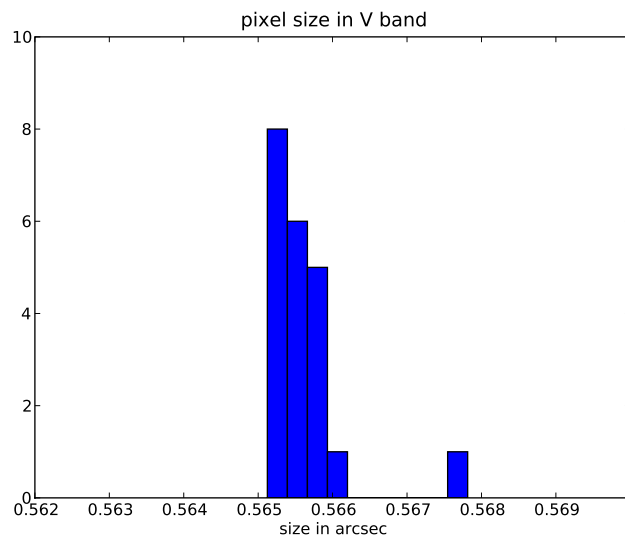
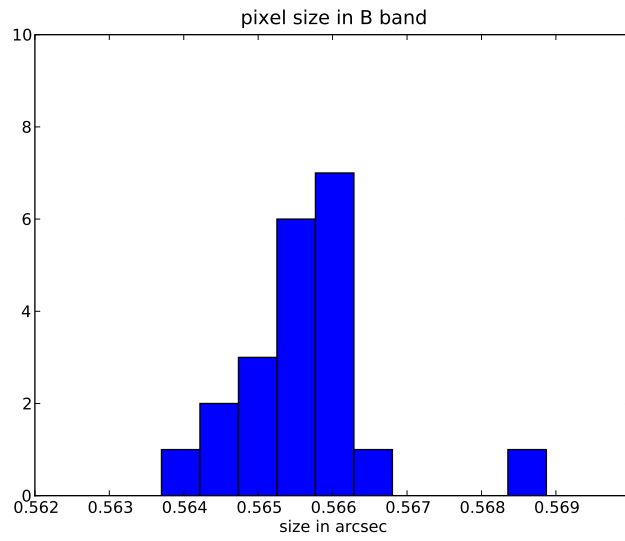
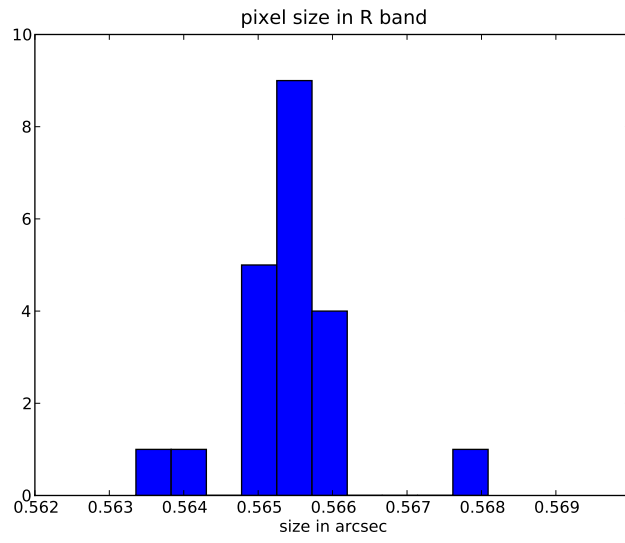


Figure 2.1: Histogram of pixel size determined from 7 stars.

The dome flats have been bias subtracted with a combination of bias frames. The two bias frames were taken before and after the dome flats. During the data reduction process no dark subtraction was done. We knew from experience that the darks are not very different from the bias frames for short exposures. A dark exposure of 20 seconds was taken and compared to the bias frame which showed that the bias frame could be used. (The mean values of counts per pixel per second differ by a factor of 1/2000.)

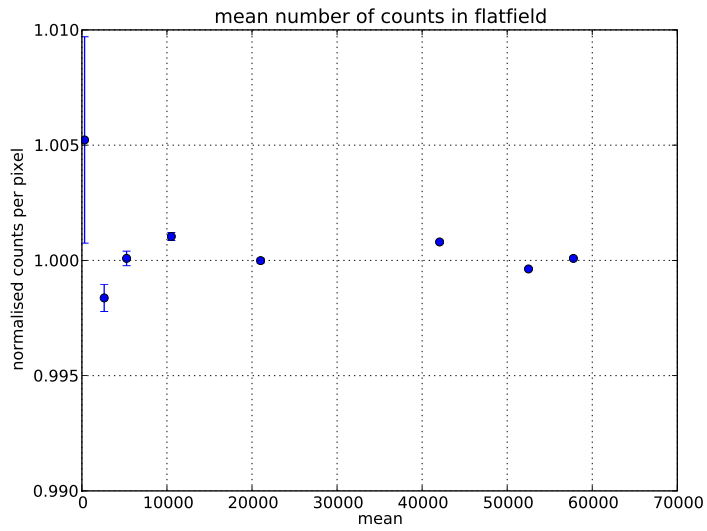
Of the flats a central part of 201 by 201 pixels was taken. First the mean and standard deviation were retrieved with *imstat* in IRAF. All the means were then divided by their exposure time. The relative deviation of these values has been plot in figure 2.2. It shows also a point at 0.12 seconds. This point was not included in the following calculations, but it is an interesting point of which more will be said later. The results are as follows: the minimum number of counts received by a pixel was 315.8, and the maximum 57783. The maximum deviation from unity was 0.0016 (see the first subplot, at 1 second) so 0.16%. From this we can expect the CCD to be linear up to 0.2% from 400 till 57000 pixels. However, when looking at the plot, it should be noticed that the errorbars are even smaller than 0.2%. How can this be explained? Because the deviations are very small, other effects than the nonlinearity of the CCD could cause deviation from unity. One of these effects might be the stability of the fluorescent light. To see whether this is a possible explanation, a small investigation was made of stable fluorescent lights. These had typical fluctuations of 0.2% and 0.5% for the Xenon and Mercury-Xenon lamp of producer Hamamatsu [5]. Another producer of stable fluorescent lights, Santec[6], sells them with a stability upto 0.5%. Because the lamp in the dome of the Gratama telescope is not even a special high stable light source, we can expect it to have fluctuations of at least this order, but it could be smaller. This explains well the small errorbars compared to the scatter of points around unity. The error in the linearity is thus less than 0.2%, which is very good for a CCD. Two of the four CCD's of the Wide Field Camera in the Isaac Newton Telescope on La Palma have for example a linearity error of 1% over the whole range [20]. The largest error arises at the end of this range, so finally their linearity is comparable to that of the Gratama Telescope.

Finally a note about the exposure of 0.12 seconds. In figure 2.2(a) it deviates from unity by 0.5% which is significantly larger than other points. This might be caused by the inaccuracy in the exposure time. The shutter of the CCD can not be opened instantaneously. It takes some time, and this inaccuracy is expected to cause the high value of the point at 0.12 seconds. This gives rise to the errorbars in the points with the shortest exposure times. It is worth testing the real accuracy of the exposure time, for example by making short exposures with times up to 0.2 second.

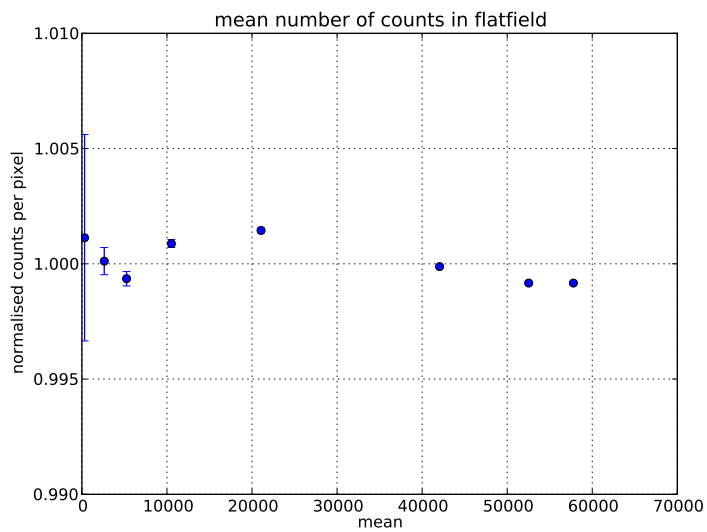
2.5 Illumination correction

2.5.1 Theory

Flat fields are made to correct for the non uniform illumination of the CCD. After flat fielding the background of the image is expected to be flat, however this is not the case. Flat fields are made with the use of diffuse light from the atmosphere. This gives a different illumination pattern from a dark night sky with some infinitely far point sources like stars. As a result, the same star detected at different places on the CCD has not the same photometric properties. Fortunately, this effect is constant in time, so once measured, it can be corrected for. (The flat fields might differ slightly with position, due to shadows from the dome for example) A star in the centre was taken as reference and the telescope moved with small steps to get the star on many places on the CCD. Now photometry was applied to that star on all positions, and their intensity divided by that of the central star is the illumination correction. A two dimensional function approximating all these differences gives the correction function.



(a)



(b)

Figure 2.2: Linearity tests done with dome flats. The points at $t=0.12$ second are not used in the calculations, but provide us with possible errors in the exposure time.

2.5.2 Practice

Normal skyflats were taken to determine the illumination correction. First 9 dark frames of an exposure time of 15 seconds were combined. The observations and flat fields of also 15 seconds were dark subtracted. Finally the flat fields were normalised to 1, combined using their median, and used for flat fielding. The airmass, which was noted on the logsheets, has been added to the headers and was used when doing photometry.

The Stetson standard field N3031 has been observed, but since the standard stars were too faint, two other stars in the area were used for this test. They have been detected at 16 places of the CCD in the R filter, a few times in the centre, and in all corners (see also figure 2.4). Photometry has been applied to these stars using IRAF. It is no problem that we have no exact information about their real magnitudes because only the relative magnitudes are needed. These stars had a FWHM of about 4.5 pixels, and in figure 2.3 the results are shown after doing photometry with an aperture of 20 pixels. Plotted is the number of counts per position on the CCD, compared with that of the central star. As can be seen, there is some structure but it is not radially symmetric (see also figure 2.4) and the maximum deviation is less than 5%. This looks reasonable, since illumination corrections can be expected to be in the order of a few percent. As an example; the ESO Wide Field Imager still has photometric errors of 5% after normal flat fielding, which can be brought down to 1% after additional illumination correction [1]. This is consistent with the result found for the Gratama telescope.

There were two similar problems with the telescope which prevented us from making a good illumination correction. First, one of the mirrors in the telescope turned out to be not perfectly fixed and was able to move during observations. This caused a bright and a dark ring in the flat fielded image. Once this problem was solved, there still appeared a small ring on the image. This ring was caused by the fact that the CCD was not perfectly fixed to the telescope and moved during observations. When the test had already been finished, a major change in the telescope was made. Because the primary mirror could still move, a plate was fixed to it. So the global illumination correction found here is not expected to be correct anymore at all.

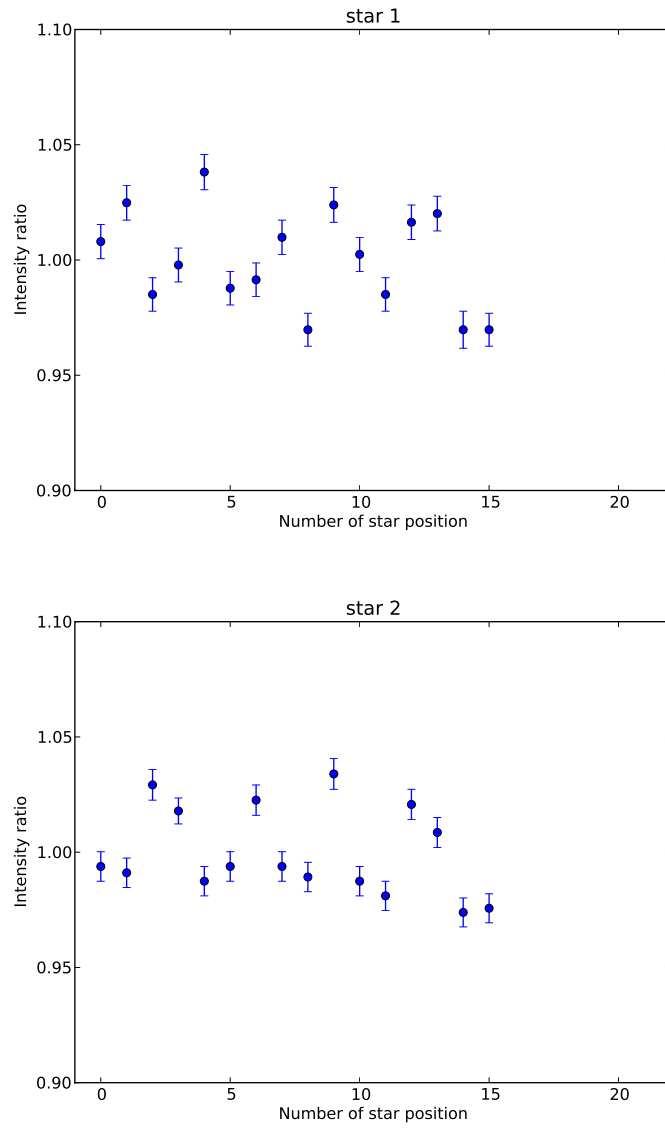


Figure 2.3: Intensity of star at different positions on the CCD, divided by that at central position. The x axis is not related to a physical place on the CCD, and photometry was done with an aperture of 20 pixels.

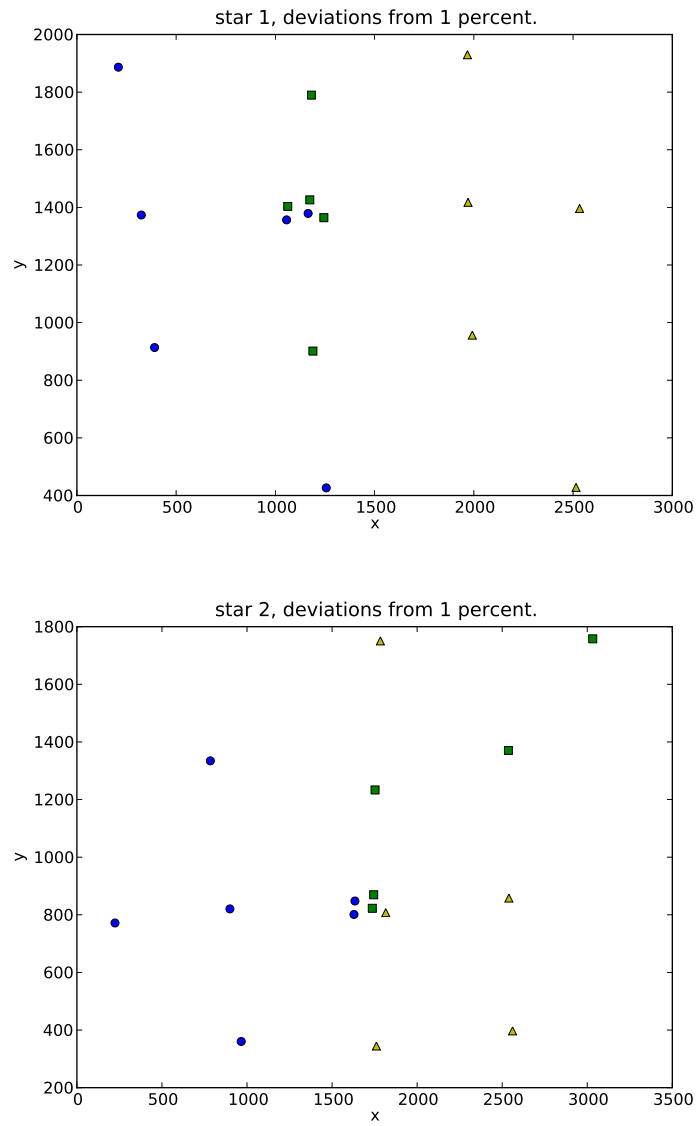


Figure 2.4: Illumination correction. Dots indicate the measured flux was less than 0.99 times the average, squares are between 0.99 and 1.01 and triangles have flux higher than 1.01 times the average.

Chapter 3

Distribution of dust in spiral galaxies

3.1 Introduction

Today, several properties of the dust distribution in spiral galaxies are known, for example that there is more dust in the disk than in the outer parts [10] [12]. It is also known that there are significant differences between galaxies, for example that the brightest galaxies in general contain most dust [13], [12]. Galaxies with absolute magnitude $M_K < -23$ are found to have a significant amount of dust, while the faint ones with $M_K > -20$ contain less [12]. The amount of dust also appears to depend on morphological type. Most dust is found in the Sc galaxies and it falls off in both earlier and later type directions [14]. It is important to have an idea of the amount of dust in galaxies, because it absorbs and scatters much of their light. This makes a galaxy look fainter and redder than it actually is, thus affecting the outcome of distance determinations and the Mass-to-light ratio [12]. To investigate the radial arm-interarm dust distribution a pilot study had been done on three galaxies by Beckman et al. [9]. Here the galaxies were separated in arms and interarms to find out whether the extinction properties differ between these two regions. A mask, containing the arms, was made in the reddest filter, and was then applied to the blue filter as well. The exponential scale lengths were determined in the whole galaxy, the arms and the interarms. Then the scale lengths in the different regions were compared. In two of the three galaxies a considerably longer scale length in the blue than in the red was found in the arms. In the interarms this difference was much smaller. This can be explained by the arms containing more dust than the interarms. The same has been done here with 23 faint and bright galaxies of different morphological types. Four models were developed by Beckman et al. to estimate the amount of dust once the scale lengths are known. One of the models will be mentioned here. It assumes a radial exponential dust distribution, scattering and absorption by dust (instead of only absorption) and a stellar to dust scale height ratio of 3.

The surface brightness of spiral galaxies is assumed to be radially exponential, in the blue as well as in the red bands. So without dust, $I = I_0 e^{-\frac{r}{h}}$, with h the scale length which depends on stellar populations, and r the radius from the centre of the galaxy. If the dust distribution is also radially exponential [12], the resulting surface brightness becomes $I = I_0 e^{-\frac{r}{h_\lambda}}$. Here h_λ is the wave length dependent scale length which depends on stellar population and extinction by dust. In a band which is almost not affected by dust, like the K band, h_λ will be close to 1. In a blue band h_λ will become larger if the galaxy contains more dust. So comparing the scale lengths is a good measure of the amount of absorbing dust. An advantage of this method is that no corrections for dust in our own galaxy have to be made, since this will not alter the slope of the surface brightness curve. Still this does not give a value for the

filter	λ_{eff} in nm
u	355
g	477
r	623
i	762
z	913

Table 3.1: A table with the effective wave lengths of the filters in the Sloan telescope

optical depth. Therefore models have been made to find the optical depth if the scale lengths are known.

3.2 Data

The images from spiral galaxies come from Sloan. Sloan is a telescope in New Mexico which has mapped one-quarter of the sky [21]. First, galaxies were first selected in RC3. RC3 is the 'third reference catalogue of bright galaxies'[16] which can be used to select galaxies on for example morphological type. Here the types 2,3,4 and 5 are selected which correspond to Sab,Sb,Sbc and Sc. Other selection criteria were $R_{25} < 0.3$ and $B_{o,T} < 13$. R_{25} is the decimal logarithm of the ratio between the two axes of the ellipse, an upper limit is set to avoid edge-on galaxies. $B_{o,T} < 13$ ensures that we select galaxies brighter than apparent magnitude 13. The catalogue returned a list with names and co-ordinates of galaxies corresponding to the criteria. These co-ordinates were used as input for the upload list of SDSS. Not all images that are returned by SDSS are useful; some contain too many foreground stars, and in some cases the galaxy is located at the edge of the image. These images were not used. The useful, corrected images (bias subtracted and flat fielded) were downloaded in all different filters (u,g,r,i,z)[8].

The filters used in Sloan are not exactly the same as the usual U,B,V,R,I filters, their effective wave length can be found in table 3.1. What do we expect to see in these filters? In general the light of the red stars will be detected in the i and z filter. This light will be least affected by dust. It is thus a good filter to use when we want to look through the dust. In the r and g filter the bluer stars are visible, and the dust absorbs and scatters a significant amount of this blue light. So comparing images in the z and the g filter should give a good idea of the dust distribution in the galaxy. A third catalogue, NED (NASA/IPAC Extragalactic Database), was used to find the absolute magnitudes of the galaxies. NED contains the distance modulus (m-M) determined with different methods and also the apparent magnitude m, so M can easily be found. The galaxies were divided in 4 types and 2 magnitudes, so in 8 bins in total. The critical magnitude has been chosen such that there were enough galaxies in all bins. Because later types tend to be fainter, the difficulty lay in having enough bright late type and faint early types galaxies. In practice this meant $M_B, crit = -20.5$.

3.3 Making masks

As explained before, the plan was to make a mask in the reddest filter (z) and apply this to the g and z filter. Since however the images turned out to be too faint in the z filter to do this, the g filter has been used instead. So first elliptical isophotes were fit to the galaxies in the g filter. This has been done as follows: Find the centre of the galaxy. A good estimate of the centre is found when one fits a Gaussian to the light distribution of the galaxy and takes the top of it. Then isophotes were fit to this galaxy with IRAF's package *galphot,surf,ellipfit*. (see [17]) The radii of the elliptical isophotes change every step with a factor 1.1, and the position angle and ellipticity are left free. This gives in general a good result but in some cases the ellipticity and

position angle vary a lot between two steps, giving an unrealistic model. In this case changing δr from 1.1 to 1.2 could help, and if this was not sufficient, the position angle and ellipticity were fixed.

Ellipfit gets an input and returns two outputs. As input it takes the original frame with the galaxy. It fits elliptical isophotes to the galaxy: these isophotes form a model which is one of the outputs. The residual, the original frame minus the model, is the other output. In the residual the arms and interarms should already be visible. This was only the case in the g and r filters. Especially the H II regions are well visible in the g filter. This is a good indication of where the arms are, because it shows the regions where young hot stars ionise hydrogen atoms which cause the H II radiation. Forcing to use the g band, one has to keep in mind the following: dust causes extinction in the g band, so if there is a lot of dust in an arm, that part will remain dark in the residual and the conclusion would be that the dusty part does not belong to an arm. In practice this caused no problems, since it is not to be expected that a whole arm will become invisible, and the final separation has been done by hand.

The different types of galaxies studied caused different problems when making a mask. As this had not been done before for a large amount of galaxies, there was not yet a standard algorithm so most of the process was done by hand. To avoid arbitrary actions and in consequent decisions a kind of algorithm has been developed after making some test masks. During this testing process most problems were indicated and solved.

The Algorithm:

1. Run *ellipfit* with the galaxy in the g and the z filter. Both with $\delta r = 1.1$ and other parameters left free.
2. Compare the residuals of both filters. (See figure 3.1(a)) Do they look the same? It is often not possible to see the arms well in the z filter but one can check at least whether arms begin at the same place. If the residuals differ a lot, the galaxy might be a barred spiral, or irregularities appear in the g filter which give a bad fit. In this case: go back to step 1 and *ellipfit* with $\delta r = 1.2$ If this does not help, then stop.
3. Look at the model. Do ellipses overlap a lot? IRAF will give a warning in that case. Go back to step 1 and *ellipfit* with $\delta r = 1.2$. If this does not help, also try to *ellipfit* with the parameters fixed. In most cases this will finally give a good result.
4. Remove the background of the model. The model often had a background of about 1000 counts.
5. Make a fraction by dividing the residual by the model. The fraction file should show the arms even better. (See figure 3.1(b))
6. Remove stars and extreme values from the fraction file. Stars are often much brighter than the rest of the residual so they are easily recognised and replaced by 0. In some cases it might be difficult to distinguish between an H II region and a star. In most cases this should not be a problem: H II regions are not as perfectly circular and have not the same light distribution as stars have. Often the residual of the fraction file contains low pixel values, for example between -5 and 5. Everything outside this range is noise, and can be replaced by 0.
7. Apply gaussian smoothing. Smoothing is done to 'glue' all the regions in the arms together and to overcome the noise. Often a smoothing factor of 2 gives the best result. In an ideal situation the area with positive values is supposed to be the arms, and the area with negative values is the interarm region. In practice this did not work so well. Especially the early types (2 and 3) still

contained too much noise to make such a definite separation. In general the arms are defined as the places where the values were larger than 1.03. These regions were connected (by hand, see step 9) to create continuous arms. As can be seen in figure 3.1(c), the noise dominates the signal especially in the outer parts of the galaxy.

8. Are the arms visible? Compare the smoothed file also with the residual in the g and z band if it is not completely clear. If there are large differences or the arms are not visible: stop.
9. Make the mask. This was done by hand with use of the program GIPSY¹ A spline function was fit to points that were marked in the file. This is the most important part of the algorithm which is not reproducible. Everything outside the mask was replaced by a value below all other values in the mask. (If the S/N of the original images are very high, and the fitting went well, then all positive values should represent the mask with the arms, and all negative values the interarms. In practice this was not the case yet.)
10. Replace everything in the mask by 1 and the rest by 0. This gives the final result. (See figure 3.1(d))

Notes on the algorithm:

- Step 3, making a model. In some cases the first model was the best one, even when it had some overlapping ellipses. This happened several times in the type 5 galaxies. In such a case the decision which model is the best one was made by eye. For example, it could happen that the first model showed some overlap, the second one showed very much overlap and the third one fits the inner part of the galaxy well but did not match the outer parts at all. In such a case the first model would be used.
- Step 4, removing the background. In a later stage the background is subtracted from the original image. If this would have been done before making the mask, this step would no longer be needed.
- Step 6, remove stars from the fraction file. Of course the stars could also be replaced before the fitting takes place. Then the light of the stars does not affect the fitting. The stars should be replaced by the mean of the values around that star. It turned out, however, that the stars were best visible in the fraction file. The best solution could be that the brightest stars are removed before ellipfitting, and smaller stars are removed from the fraction file.
- The actual making of the mask, step 9, was now done by hand because the signal is too low to do it automatically. It would be better if this could be done automatically. An option is: observing again, making sure that the signal to noise ratio is much higher. Or combining the light from all the filters. Just adding the images in different filters will probably not help much. The g filter dominates the z filter and most information from the z filter will be lost. The problem remains in the residuals, but adding or averaging fraction files might help.

The galaxies of which a mask has successfully been made are found in table 3.2. The images showing the arms and interarm regions are given in Appendix C.

¹Groningen Image Processing SYstem is a program made at the Kapteyn Astronomical Institute, university of Groningen. Documentation can be found at <http://www.astro.rug.nl/gipsy/>

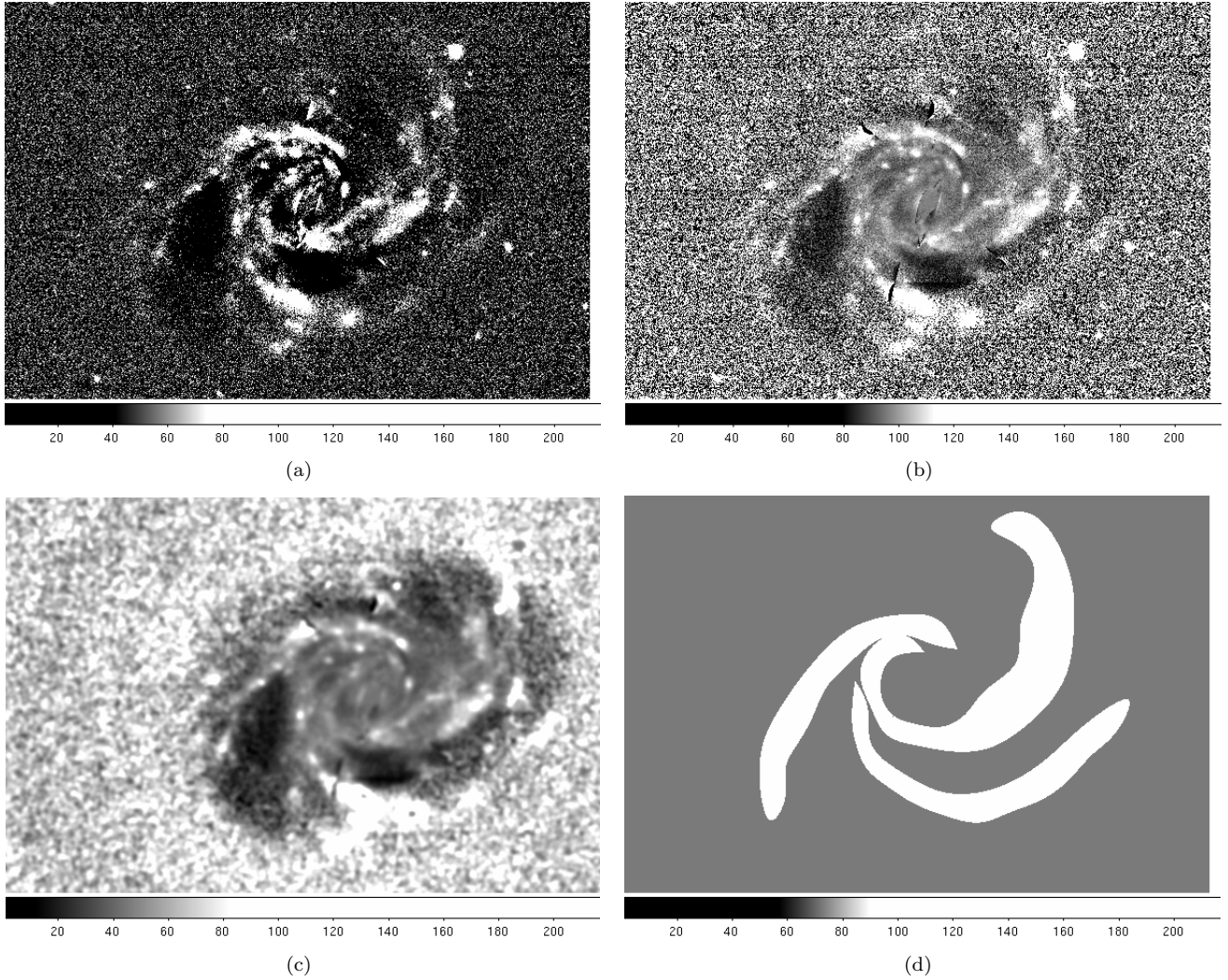


Figure 3.1: Four different stages from the algorithm; the residue, fraction file, smoothed file and the final mask.

	T2	T3	T4	T5
$M_B < -20.5$ mag	UGC 4820 UGC 6118 UGC 9133	MCG-1-33-13 UGC 2200 UGC 7067	UGC 7067 UGC 7225 UGC 9334 UGC 9481	ESO 569-22 MCG-1-35-16 UGC 438
$M_B > -20.5$ mag	UGC 5731 UGC 6787	UGC 12702 UGC 7753 UGC 9915	UGC 7884 UGC 4503	UGC 12788 UGC 5887 UGC 6484

Table 3.2: An overview of all galaxies of which a mask has been made.

3.4 Scale lengths

When the masks were made, some preparations had to be taken before the final fitting could be done. The background of the original image was subtracted (this could have been done before as well). Then the image was separated in an arm and an interarm region, according to the mask. From the isophotes of the first fitting session the average position angle and ellipticity is taken as input for the final fitting. These give, together with the centre of the galaxy, the model for the fitting. *Ellipfit* was used again to get the residual image and a table with the average intensity per pixel I in the ellipse as function of radius r . From the table, a plot of $\log(I)$ as function of r was made. Since the intensity profile of the galaxies is approximately described by $I(r) = I_0 e^{-\frac{r}{h_\lambda}}$, the line will show a straight line. In practice the plot will show the bulge in the centre, a straight line in the disk, and sometimes a straight line with a different slope in the outer parts of the galaxy. The slope of the line is $-\frac{1}{h_\lambda}$ and the scale length in the different filters can thus be found. A line has been fit to the plot using the least squares method. After this process the scale lengths in the g filter can be compared with those in the z filter.

Changing the range of the fit can significantly affect the outcome. This was already known from the pilot by Beckman et al, and it was noticed by us as well. For this reason an error was introduced in the following way: After the range was decided upon, a second fit was made with only the first 80 % of the data points, and a third fit with only the last 80 %. Now the average of the three resulting scale lengths was taken, with the standard deviation as a measure of the error. In the end, not the individual scale lengths will be used, but the ratios of them. The error in the ratios is expected to be less dependent on the range, so these errors are probably overestimated. (see Appendix D for the numerical results) Another important thing to keep in mind when choosing the range is the error in $\log(I)$. The background of the original images is not completely flat, it has systematic deviations of about 1 count. This is important if the intensity in the arms and interarms becomes small. For this reason, a small range in which the data was reliable has been chosen in some cases. Another point to note is the fact that the mask in two type 3 galaxies covered the outer part of the galaxy. It was then very difficult to separate arms and interarm regions close to the centre of the galaxy. The results are still used, but probably give lower ratios than expected. For the resulting plots, see Appendix E. The numerical results are given in Appenix D.

3.5 The model

Once the scale lengths are known, these can be compared to a model. One of the models of Beckman et al. has been used here, see reference [9] and the right part of figure 3.2. It assumes that dust absorbs and scatters the light, and that it is exponentially distributed in the galaxy with a scale height above the plane three times less than the scale height of the stars. This was done because it is the case in our own galaxy [23]. The model predicts the change in radial intensity scale length for wave lengths between 300 and 2300 nanometre as a function of optical depth τ_ν . Table 3.3 shows the relevant parameters. These were derived from figure 3.2. The ratios $\frac{R_{obs}}{R_s}$ were read from the figure at $\lambda = 0.48\mu$ for the g and at $\lambda = 0.91\mu$ for the z filter. Dividing these values gives the results in table 3.3. The model makes an important assumption: it assumes the dust scale height to be one third of the stellar scale height. As a result a significant part of the stellar light will not be affected by dust at all. This results in relatively low scale length ratios. (See table 3.3) Another consequence of this model is that, for high values optical depths, the scale length ratio is not always increasing with increasing optical depth. So if the results show a ratio of 1.18, the only conclusion that can be drawn is that the optical depth is high. In the original paper by Beckman et al. more than two bands were used. The

τ_ν	20	10	4	2	1
$\frac{h_g}{h_z}$	1.17	1.20	1.09	1.08	1.01

Table 3.3: The ratio in scale lengths in g and z filter for some values of optical depth, according to the model.

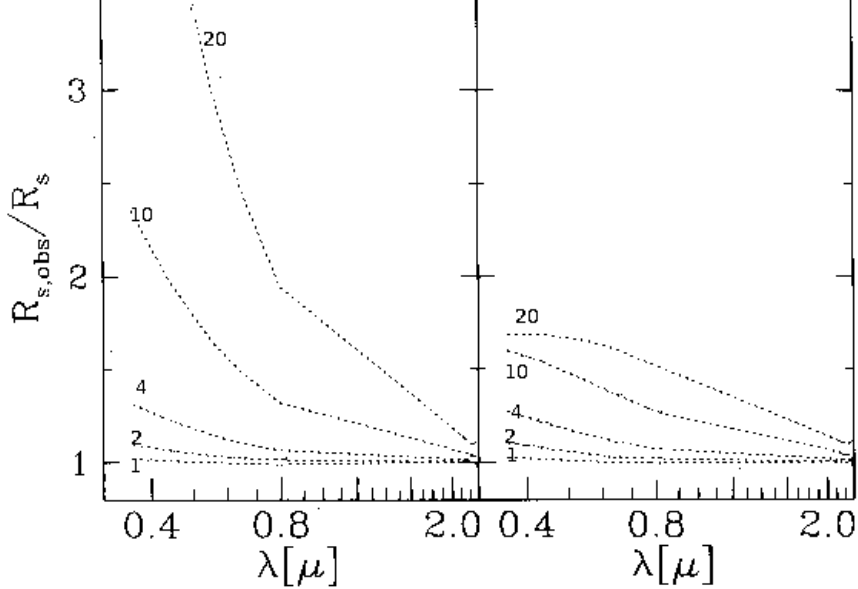


Figure 3.2: Two models from Beckman et al: The scale length ratio is given as function of wave length. Left without scattering, right with scattering. The right one was used for table 3.3.

combination of ratios in four bands would give much more information already. In that case the scale length ratio can be plotted as function of wave length and a more reliable statement about the optical depth could be made.

3.6 Results

The results have been summarised in table 3.4. It shows the averaged scale length ratios for different types and luminosities, corrected for metallicity gradients (see next section). Because there are only a few galaxies in each box, the statistical significance is not very high. The table can be used, however, to see some trends. The scale length ratio seems to grow with type, which was expected. In all cases the ratio in the arms is higher than in the interarms which gives the strong suggestion that there is a significant difference in amount of dust between arms and interarms. Also this was expected. However, there is no clear difference between bright and faint galaxies. The relatively large errors arise because of the differences in ratios from galaxy to galaxy. In Appendix D the individual results are given which have smaller errors.

How do these results compare to the model? It gives a maximum scale length ratio of 1.20, and our results also have a maximum at about 1.20. That is in favour of the model. It would give the following interpretation to our results: The dust in the interarm regions has an optical depth varying from 1 (for T2) to 5 (for T5). In the arms the optical depth varies from 1 (for T2) to 20 or more (for T4 and T5). These are rough estimations. To be able to say something more significant about the real optical depth, the same procedure has to be done in two other bands.

	T2	T3	T4	T5
$M_B < -20.5$ mag, arms	1.05 ± 0.08	1.03 ± 0.08	1.18 ± 0.11	1.21 ± 0.08
$M_B < -20.5$ mag, interarms	1.03 ± 0.08	0.95 ± 0.09	1.02 ± 0.03	1.14 ± 0.08
$M_B > -20.5$ mag, arms	1.00 ± 0.03	1.05 ± 0.04	1.13 ± 0.07	1.22 ± 0.12
$M_B > -20.5$ mag, interarms	0.96 ± 0.01	1.02 ± 0.07	1.02 ± 0.08	1.08 ± 0.06

Table 3.4: Average scale length ratios for different types and luminosities, corrected for metallicity abundance gradients. See also appendix D for the individual results.

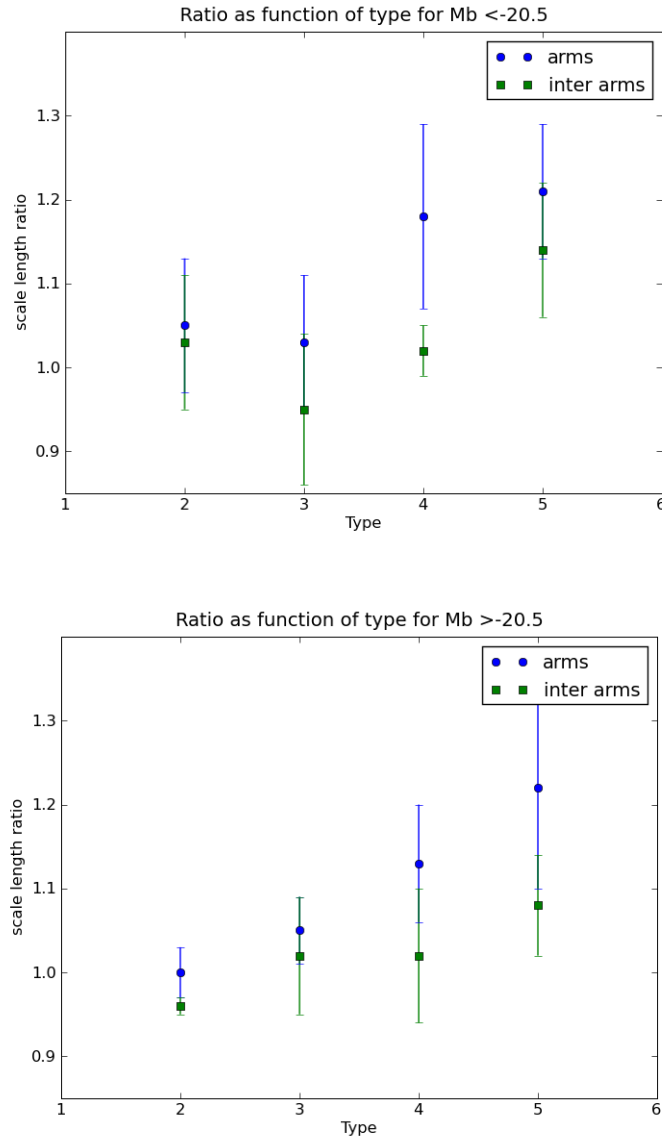


Figure 3.3: Scale length ratios as function of type, arm/interarms region and luminosity.

3.6.1 Metallicity

Dust is not the only factor that can cause the difference between scale lengths. Also radial metallicity abundance gradients could do that. If the metallicity abundance in the inner part of a galaxy is larger than at a larger radius, the scale length in the red will become smaller. So without correction for this, the amount of dust in the galaxy will be overestimated. A study from Zaritsky et al. (1994) [18] shows that these gradients are small and do not depend on Hubble type, so we can correct for all of them in the same way. The gradient in abundance is about -0.2 dex/scale length, which is $10^{-0.2} = 0.63$ difference in metallicity abundance per scale length. This is a rough approximation, it can be different for every galaxy so the correction will only be useful on the average of all galaxies. The next question is how this difference in metallicity abundance translates into colour differences. For this the tables of Bruzual and Charlot [19] were used (from a programme called GalaxEV). Of the two available stellar models, Chabrier has been used with $\log(\text{age}) = 10$. The z band in Sloan is the same as their I band, and the g band is in between their V and B band. So from B-V and V-I in the table, the difference in magnitude in the g and z band because of metallicity can be deduced. This translates in a small correction factor for the scale length in the z band of 1.06. The data presented in 3.4 and Appendix D have been corrected this way. Note that it is assumed that the metallicity gradient in the arms is the same as in the interarms, possible differences are not taken into account. This might be an explanation of the fact that the ratios in table 3.4 are in some cases below 1 (which is not expected). It is also possible that there are star forming regions in the inner part of some early type galaxies, and in the outer part of late type galaxies. These would also cause lower scale length ratios than expected.

3.6.2 Sample discussion

It is always important to check whether the results are affected by parameters that were not taken into account. One important parameter in this case is the inclination angle. If a galaxy is inclined, the light from the part furthest away will have to travel through more dust, and will thus be affected more by extinction. So the scale length ratio is expected to be larger when i is larger, and this ratio should approximately be linear related to $\cos(i)$. Figure 3.4 shows no clear dependence of $\frac{h_a}{h_z}$ on $\cos(i)$, so the ratios can safely be compared with each other.

3.7 Conclusion

The whole concept of separating arms and interarms seems useful, since significant differences between scale length ratios in both parts are found. They confirm the expectation that arms contain more dust than interarms. Also the expectation that more dust is found in later type galaxies was satisfied. Only no clear difference between bright and faint galaxies was found.

The drawback of this concept for future use is that separating the arms from the interarms is time consuming and that no way has been found yet to do this automatically. For a few galaxies it is possible to do everything by hand, but to get statistically significant answers, many galaxies should be used.

At last it would have been informative to translate the scale length ratios to optical depths. This appears to be difficult with the model currently used. To be able to say more about these optical depths, the procedure should be done in one or two other filters as well, and preferably also in the near infrared. Since the masks for the galaxies used here are already available, it could be done quite easily with this set of galaxies. Those results would be a good test for the model, or could possibly be used to improve it.

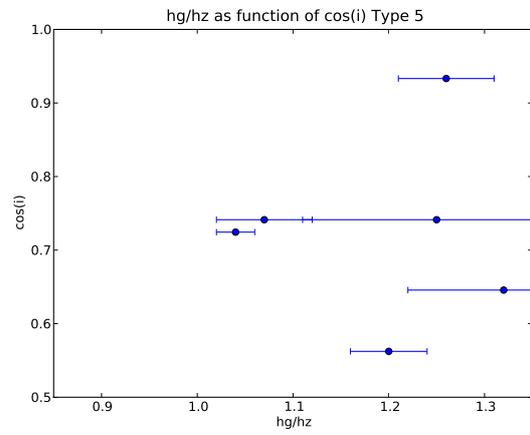
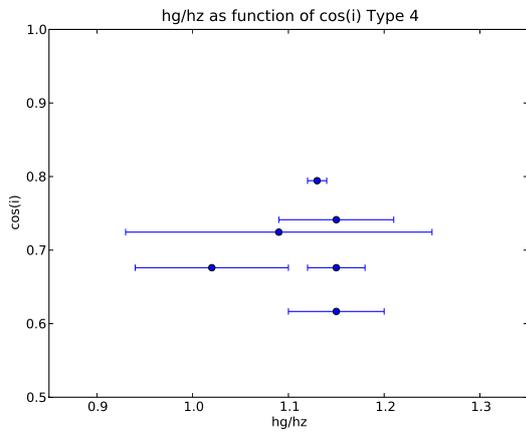
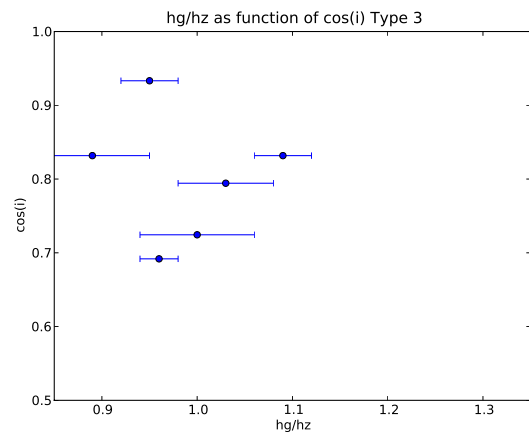
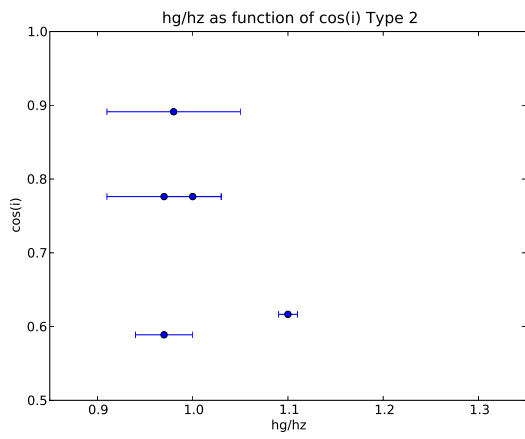


Figure 3.4: plot of $\frac{h_g}{h_z}$ versus $\cos(i)$

Acknowledgements

I would like to thank Reynier Peletier for being my supervisor, helping me through all the stages of this research project and giving a lot of background information. Also I thank Marc Verheijen for helping me doing observations with the Gratama telescope and giving interpretations to the results. Finally, this research project could not have been done without SDSS.

Funding for the SDSS and SDSS-II has been provided by the Alfred P. Sloan Foundation, the Participating Institutions, the National Science Foundation, the U.S. Department of Energy, the National Aeronautics and Space Administration, the Japanese Monbukagakusho, the Max Planck Society, and the Higher Education Funding Council for England. The SDSS Web Site is <http://www.sdss.org/>. The SDSS is managed by the Astrophysical Research Consortium for the Participating Institutions. The Participating Institutions are the American Museum of Natural History, Astrophysical Institute Potsdam, University of Basel, University of Cambridge, Case Western Reserve University, University of Chicago, Drexel University, Fermilab, the Institute for Advanced Study, the Japan Participation Group, Johns Hopkins University, the Joint Institute for Nuclear Astrophysics, the Kavli Institute for Particle Astrophysics and Cosmology, the Korean Scientist Group, the Chinese Academy of Sciences (LAMOST), Los Alamos National Laboratory, the Max-Planck-Institute for Astronomy (MPIA), the Max-Planck-Institute for Astrophysics (MPA), New Mexico State University, Ohio State University, University of Pittsburgh, University of Portsmouth, Princeton University, the United States Naval Observatory, and the University of Washington.

Bibliography

- [1] Manfroid J., Selman F.J., Jones H., Achieving 1 % photometric accuracy with the ESO wide field imager, ESO messenger 104,16,2001
- [2] Landolt,UBVRI standards,AJ,104,340,1992
- [3] SBIG Astronomical products, Product Catalog, october 16 2007
- [4] <http://www.rug.nl/sterrenkunde/sterrenwacht/index> (31-11-2009)
- [5] light source catalog, (TLSO0003E02, sep 2008 IP3000)
- [6] <http://www.santec.com/products/lasers/lasersTSL-210V.htm> (01-03-2009)
- [7] Stetson P.B.,Homogeneous Photometry for Star Clusters and Resolved Galaxies. Photometric Standard Stars ,PASP, 112, 925, 2000
- [8] Gunn J.E. et al. The sloan digital sky survey photometric camera, 1998, AJ,116,3040
- [9] Beckman J.E., Peletier R.F., Knapen J.H., Corradi R.L.M., Scale lengths in disk surface brightness as probes of dust extinction in three spiral galaxies: M51, NGC 3631, and NGC 4321, ApJ, 467,175,1996
- [10] Peletier R.F., Valentijn E.A., Moorwood A.F.M., Freudling W., Knapen J.H., Beckman J.E.,The extinction by dust in the outer parts of spiral galaxies,A&A, 300,L1, 1995
- [11] Valentijn E.A.,Opaque spiral galaxies, Nature, 346,153,1990
- [12] Tully R.B., Pierce M.J., Huang J., Saunders W., Verheijen M.A.W., Witchalls P.L.,Global extinction in spiral galaxies, AJ,115,2264,1998
- [13] Giovanelli R., Haynes M.P., Salzer J.J., Wegner G., Da Costa L.N., Freudling W., Dependence on luminosity of photometric properties of disk galaxies: surface brightness, size, and internal extinction, AJ, 110,1059,1995
- [14] Peletier R.F., Valentijn E.A., Moorwood A.F.M., Freudling W., The distribution of dust in Sb's and Sc's , A&A, supplement series 108:621,1994
- [15] Bartolomeo A.D., Barbaro G., Perinotto M.,Internal extinctions in spiral disk galaxies, 1995, RAS, 277,1279
- [16] de Vaucouleurs G., de Vaucouleurs A., Corwin H.G.Jr, Buta R. J., Paturel G., Fouqué P., Third Reference Catalogue of Bright Galaxies. Springer-Verlag (RC3),1991
- [17] Jørgensen I.,Franx M.,Kjærgaard P.,CCD surface photometry for E and S0 galaxies, A&AS,95,489,1992
- [18] Zaritsky D.,Kennicutt R.C., Huchra J.P., H II regions and the abundance properties of spiral galaxies,ApJ. 420, 87-109, 1994

- [19] Bruzual G. ,Charlot S.,Stellar population synthesis at the resolution of 2003 ,
MNRAS 344,1000,2003
- [20] <http://www.ast.cam.ac.uk/wfcsur/technical/foibles/index.php> (31-11-2009)
- [21] Abazajian K., The First Data Release of the Sloan Digital Sky Survey, AJ, 126,
2081-2086,2003
- [22] Disney M., Davies J.,Phillips S., Are galaxy discs optically thick?,
MNRAS,239,939-976,1989
- [23] Kent S.M.,Dame T.M., Fazio G., Luminosity models of milky way, ApJ,378:131-
138,1991

Appendix A

Data Gratama telescope

For users of the computernetwork at the Kapteyn institute, it is possible to access all data obtained with the Gratama telescope. Simply go to:
/net/vega/data/users/observatory/images/ , add the date of observations like 081210 for the 10th of December 2008, and go to STL-6303E for photometry instead of spectroscopy, and to /i for the imaging CCD (instead of the tracking CCD).

date	objects	use
27-09-2008	SA113, flats,darks	pixel size
06-03-2009	domeflats,darks	linearity
19-03-2009	darks,flats, NGC3031	illumination correction

Appendix B

STL-6303E Typical Specifications

Imaging CCD	Kodak Enhanced KAF-6303E
Pixel Array	3072 x 2048 pixels, 27.5 x 18.4 mm
Total Pixels	6.3 million
Pixel Size	9 x 9 microns
Full Well Capacity (NABG)	100,000 e-
Dark Current	0.3 e-/pixel/second at 0 degrees C
Antiblooming	NABG standard, ABG optional
Shutter	Electromechanical
Exposure	0.12 to 3600 seconds, 10ms resolution
Correlated Double Sampling	Yes
A/D Converter	16 bits
A/D Gain	1.4e-/ADU unbinned, 2.3e- binned
Read Noise	13.5e- RMS
Binning Modes	1 x 1, 2 x 2, 3 x 3
Full Frame Download	15 seconds
Cooling - standard	Two-Stage Thermoelectric, Water Assist, -40 C from Ambient Typical
Temperature Regulation	0.1C
Power	10 - 18VDC, 12VDC nominal, Universal AC to 12VDC desktop supply
Computer Interface	USB 1.1
Computer Compatibility	Win 98 / NT / 2000 / Me / XP / Mac OS-X / Vista 32 bit / Linux (3rd party)
Guiding	Dual CCD Self-Guiding Standard, Remote Guiding Head Optional
Dimensions	6.5 x 6 x 3.5" (16.5 x 15.2x8.9cm)
Weight	4 pounds (1.8 Kg) without filters
Internal Filter Carousel	5 positions for 48mm threaded cells or 2" unmounted filters (optional)
Mounting	2" nosepiece included
Backfocus	Approximately 1.7 inches (4.3 cm) with 2" nosepiece attached

Appendix C

Galaxies

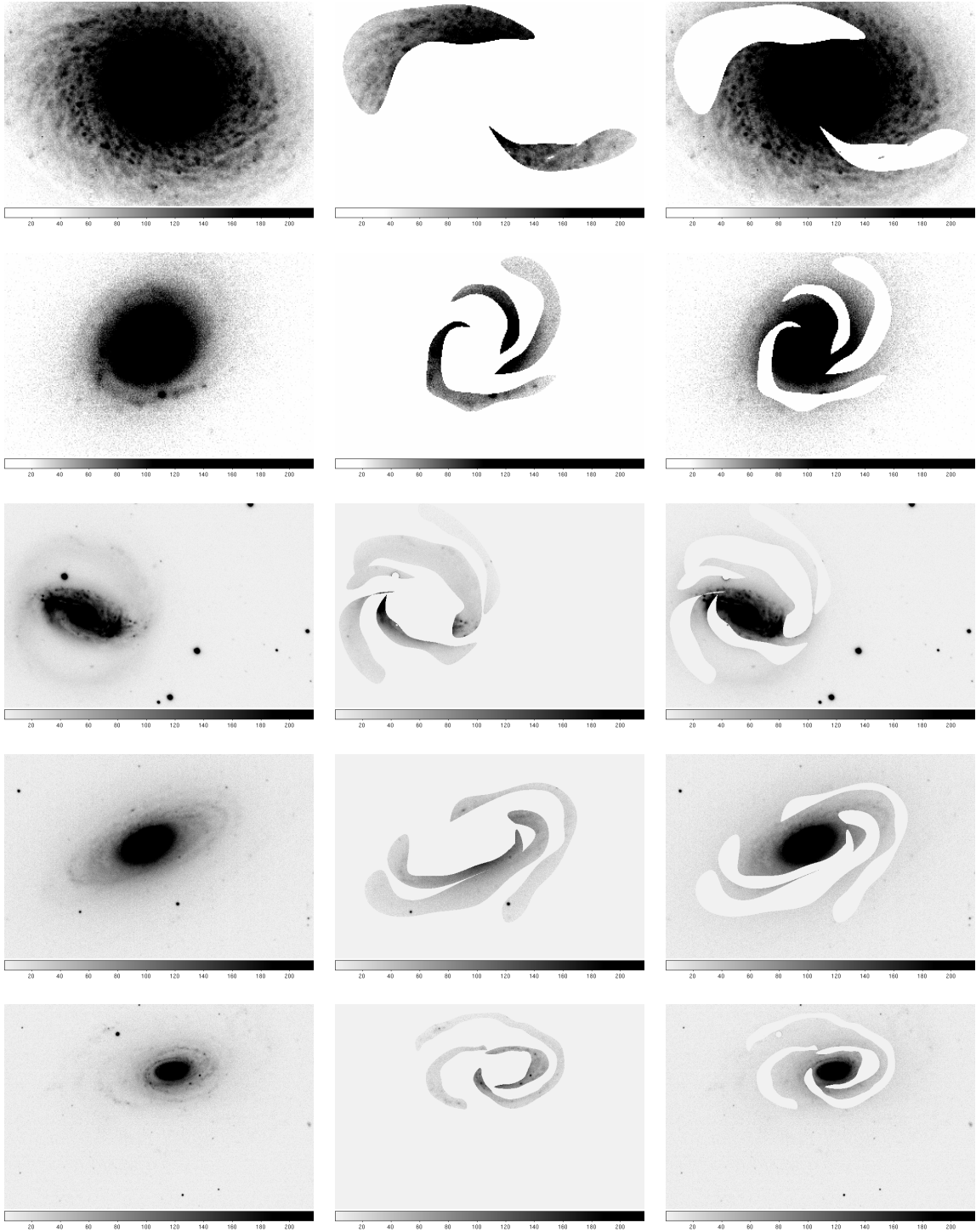


Figure C.1: Type 2 residuals. Total, arms, interarms

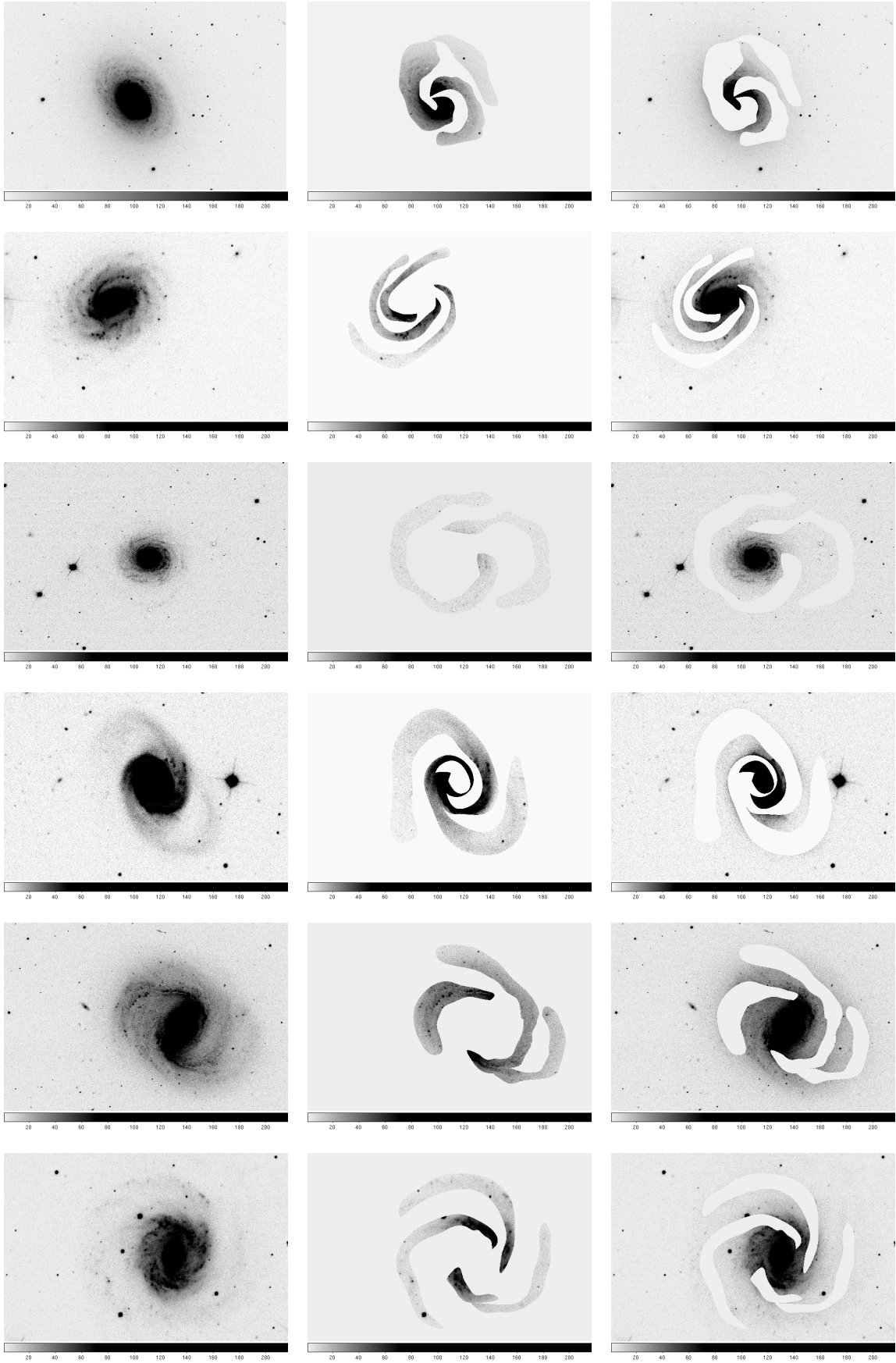


Figure C.2: Type 3 residuals: Total, arms, interarms

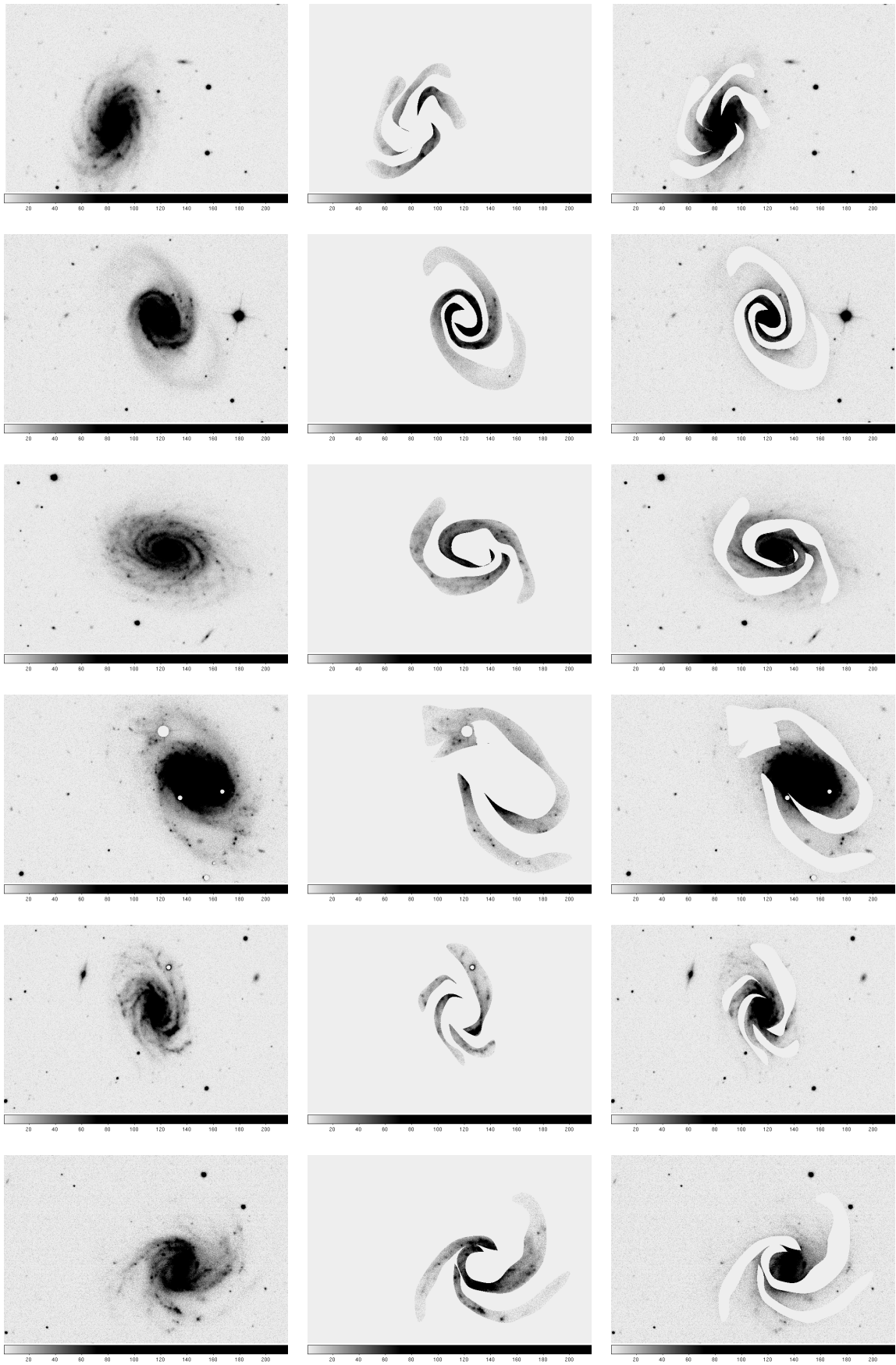


Figure C.3: Type 4 residuals: Total, arms, interarms

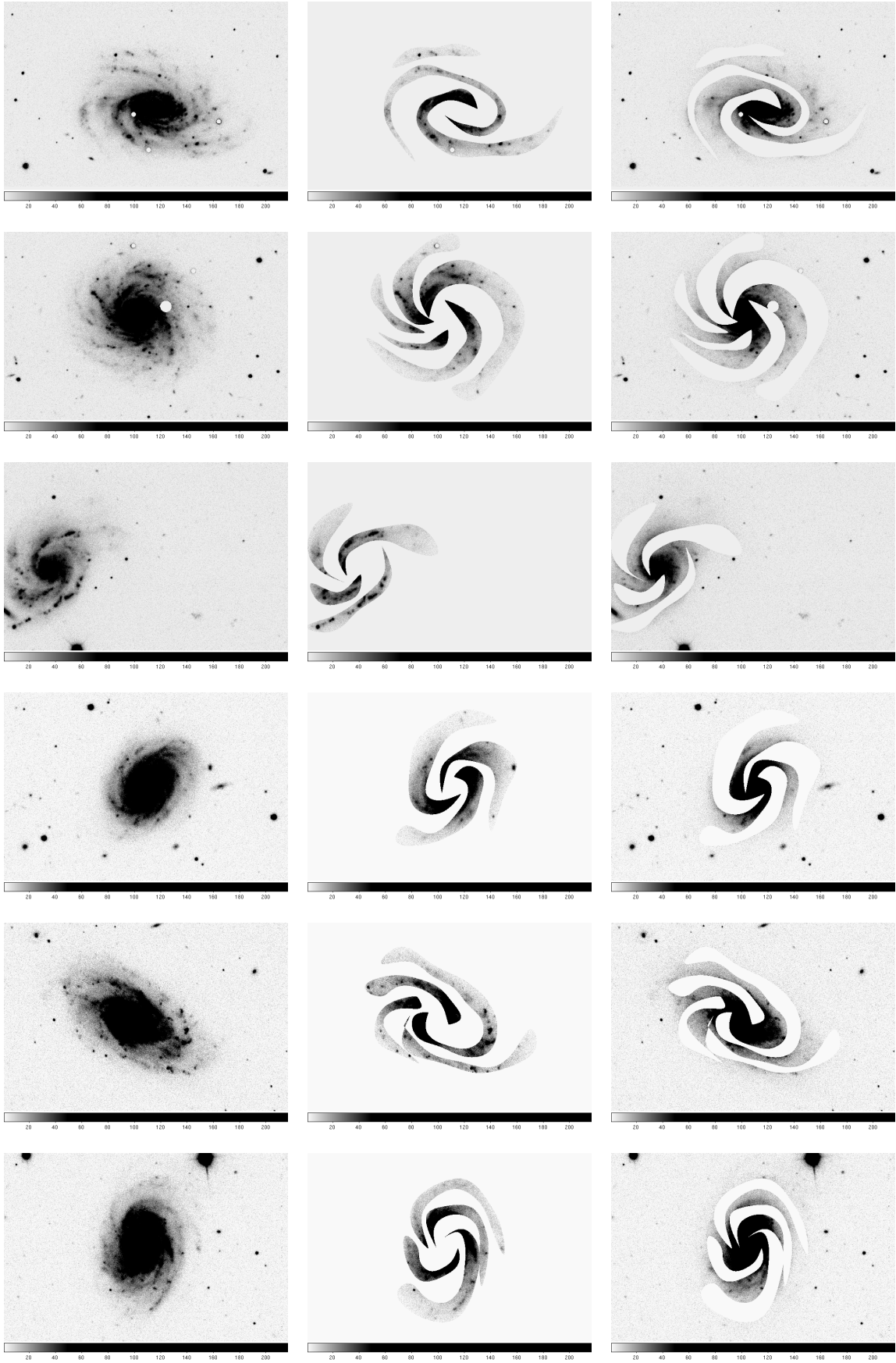


Figure C.4: Type 5 residuals: Total, arms, interarms

Appendix D

Least squares fits: tables

UGC 4820	part	hg	hz	$\frac{hg}{hz}$
	total	25.6 ± 0.6	25.5 ± 0.5	1.00 ± 0.03
	arms	30.9 ± 1.3	31.0 ± 0.2	1.00 ± 0.04
	interarms	24.9 ± 0.5	24.9 ± 0.4	1.00 ± 0.03
	$\frac{h2}{h3}$	1.24 ± 0.06	1.24 ± 0.02	
UGC 5731	part	hg	hz	$\frac{hg}{hz}$
	total	8.3 ± 0.5	8.5 ± 0.4	0.98 ± 0.07
	arms	8.9 ± 0.5	8.7 ± 0.4	1.02 ± 0.08
	interarms	8.1 ± 0.5	8.4 ± 0.4	0.96 ± 0.07
	$\frac{h2}{h3}$	1.09 ± 0.09	1.03 ± 0.07	
UGC 6118	part	hg	hz	$\frac{hg}{hz}$
	total	19.7 ± 1.0	20.3 ± 0.8	0.97 ± 0.06
	arms	29.4 ± 1.5	30.0 ± 1.3	0.98 ± 0.07
	interarms	16.5 ± 0.3	17.1 ± 0.2	0.96 ± 0.02
	$\frac{h2}{h3}$	1.79 ± 0.10	1.75 ± 0.08	
UGC 6787	part	hg	hz	$\frac{hg}{hz}$
	total	25.0 ± 0.5	25.9 ± 0.6	0.97 ± 0.03
	arms	26.8 ± 1.5	27.8 ± 1.4	0.97 ± 0.07
	interarms	24.3 ± 0.3	25.1 ± 0.5	0.97 ± 0.02
	$\frac{h2}{h3}$	1.10 ± 0.06	1.11 ± 0.06	
UGC 9133	part	hg	hz	$\frac{hg}{hz}$
	total	15.5 ± 0.1	14.1 ± 0.1	1.10 ± 0.01
	arms	16.9 ± 0.3	14.5 ± 0.3	1.16 ± 0.03
	interarms	16.6 ± 0.1	14.5 ± 0.2	1.14 ± 0.01
	$\frac{h2}{h3}$	1.02 ± 0.02	1.00 ± 0.02	

Table D.1: scale lengths of the Type 2 galaxies

MCG-1-33-13	part	hg	hz	$\frac{hg}{hz}$
	total	11.0 ± 0.1	11.4 ± 0.2	0.96 ± 0.02
	arms	10.8 ± 0.3	11.0 ± 0.3	0.98 ± 0.03
	interarms	11.1 ± 0.1	11.9 ± 0.2	0.93 ± 0.01
	$\frac{h2}{h3}$	0.97 ± 0.02	0.92 ± 0.03	
UGC 12702	part	hg	hz	$\frac{hg}{hz}$
	total	15.4 ± 0.5	14.1 ± 0.1	1.09 ± 0.03
	arms	16.0 ± 0.5	14.4 ± 0.1	1.11 ± 0.04
	interarms	14.8 ± 0.4	13.8 ± 0.1	1.07 ± 0.03
	$\frac{h2}{h3}$	1.08 ± 0.04	1.05 ± 0.01	
UGC 2200	part	hg	hz	$\frac{hg}{hz}$
	total	20.9 ± 0.9	23.4 ± 1.1	0.89 ± 0.06
	arms	30.2 ± 0.8	31.6 ± 0.5	0.96 ± 0.03
	interarms	18.7 ± 0.6	21.6 ± 1.0	0.86 ± 0.05
	$\frac{h2}{h3}$	1.61 ± 0.07	1.46 ± 0.07	
UGC 7067	part	hg	hz	$\frac{hg}{hz}$
	total	12.2 ± 0.6	12.1 ± 0.5	1.00 ± 0.06
	arms	14.5 ± 0.6	12.7 ± 0.6	1.14 ± 0.07
	interarms	11.1 ± 0.4	10.4 ± 0.3	1.07 ± 0.05
	$\frac{h2}{h3}$	1.31 ± 0.07	1.23 ± 0.07	
UGC 7753	part	hg	hz	$\frac{hg}{hz}$
	total	51.4 ± 1.5	49.8 ± 1.7	1.03 ± 0.05
	arms	41.0 ± 1.3	40.5 ± 0.9	1.01 ± 0.04
	interarms	53.6 ± 2.2	50.7 ± 2.5	1.06 ± 0.07
	$\frac{h2}{h3}$	0.77 ± 0.04	0.80 ± 0.04	
UGC 9915	part	hg	hz	$\frac{hg}{hz}$
	total	15.6 ± 0.4	16.5 ± 0.3	0.95 ± 0.03
	arms	15.9 ± 0.3	15.4 ± 0.2	1.03 ± 0.03
	interarms	15.6 ± 0.3	17.0 ± 0.3	0.92 ± 0.03
	$\frac{h2}{h3}$	1.02 ± 0.03	0.91 ± 0.02	

Table D.2: scale lengths of the Type 3 galaxies. In UGC 2200 and UGC 7753 the mask covered only the outer parts of the galaxy. This probably gives lower ratios than expected.

	part	hg	hz	$\frac{hg}{hz}$
UGC 4503	total	14.5 ± 0.6	12.6 ± 0.3	1.15 ± 0.05
	arms	15.9 ± 0.8	13.2 ± 0.5	1.20 ± 0.08
	interarms	13.0 ± 0.4	12.0 ± 0.1	1.09 ± 0.03
	$\frac{h2}{h3}$	1.22 ± 0.07	1.11 ± 0.04	
	part	hg	hz	$\frac{hg}{hz}$
UGC 7067	total	13.4 ± 1.7	12.3 ± 1.0	1.09 ± 0.16
	arms	13.9 ± 1.3	13.6 ± 0.8	1.02 ± 0.11
	interarms	11.9 ± 1.5	11.6 ± 0.4	1.03 ± 0.13
	$\frac{h2}{h3}$	1.16 ± 0.18	1.17 ± 0.08	
	part	hg	hz	$\frac{hg}{hz}$
UGC 7225	total	19.1 ± 0.8	16.6 ± 0.4	1.15 ± 0.06
	arms	23.7 ± 0.8	19.9 ± 0.3	1.19 ± 0.05
	interarms	16.2 ± 0.9	15.3 ± 0.5	1.06 ± 0.07
	$\frac{h2}{h3}$	1.46 ± 0.09	1.30 ± 0.05	
	part	hg	hz	$\frac{hg}{hz}$
UGC 7884	total	13.5 ± 0.8	13.3 ± 0.7	1.02 ± 0.08
	arms	19.0 ± 0.8	17.9 ± 0.7	1.06 ± 0.06
	interarms	11.8 ± 0.5	12.6 ± 0.7	0.94 ± 0.07
	$\frac{h2}{h3}$	1.61 ± 0.10	1.42 ± 0.10	
	part	hg	hz	$\frac{hg}{hz}$
UGC 9334	total	13.0 ± 0.2	11.3 ± 0.2	1.15 ± 0.03
	arms	23.1 ± 0.2	17.6 ± 0.6	1.31 ± 0.05
	interarms	10.8 ± 0.4	10.9 ± 0.2	1.00 ± 0.04
	$\frac{h2}{h3}$	2.13 ± 0.08	1.62 ± 0.06	
	part	hg	hz	$\frac{hg}{hz}$
UGC 9481	total	14.8 ± 0.1	13.1 ± 0.1	1.13 ± 0.01
	arms	21.2 ± 0.6	17.8 ± 0.7	1.19 ± 0.05
	interarms	12.3 ± 0.6	12.5 ± 0.8	0.98 ± 0.08
	$\frac{h2}{h3}$	1.72 ± 0.09	1.42 ± 0.11	

Table D.3: scale lengths of the Type 4 galaxies

ESO 569-22	part	hg	hz	$\frac{hg}{hz}$
	total	19.3 ± 1.2	14.6 ± 0.5	1.32 ± 0.10
	arms	19.3 ± 1.7	15.6 ± 0.8	1.24 ± 0.12
	interarms	16.7 ± 0.3	13.7 ± 0.3	1.22 ± 0.04
	$\frac{h2}{h3}$	1.16 ± 0.10	1.14 ± 0.06	
MCG-1-35-16	part	hg	hz	$\frac{hg}{hz}$
	total	21.0 ± 0.7	16.7 ± 0.3	1.26 ± 0.05
	arms	22.4 ± 0.8	17.4 ± 0.2	1.29 ± 0.05
	interarms	18.3 ± 0.7	15.6 ± 0.2	1.18 ± 0.05
	$\frac{h2}{h3}$	1.23 ± 0.06	1.12 ± 0.02	
UGC 12788	part	hg	hz	$\frac{hg}{hz}$
	total	21.6 ± 2.0	17.3 ± 1.2	1.25 ± 0.14
	arms	23.5 ± 4.4	18.5 ± 2.3	1.27 ± 0.29
	interarms	18.0 ± 0.8	16.2 ± 0.9	1.11 ± 0.08
	$\frac{h2}{h3}$	1.30 ± 0.25	1.14 ± 0.16	
UGC 438	part	hg	hz	$\frac{hg}{hz}$
	total	11.7 ± 0.3	11.0 ± 0.4	1.07 ± 0.05
	arms	12.3 ± 0.4	11.2 ± 0.4	1.10 ± 0.05
	interarms	11.2 ± 0.3	10.9 ± 0.4	1.03 ± 0.04
	$\frac{h2}{h3}$	1.09 ± 0.04	1.02 ± 0.05	
UGC 5887	part	hg	hz	$\frac{hg}{hz}$
	total	12.9 ± 0.3	10.7 ± 0.2	1.20 ± 0.04
	arms	13.5 ± 0.2	10.2 ± 0.2	1.33 ± 0.03
	interarms	12.1 ± 0.5	10.6 ± 0.5	1.13 ± 0.07
	$\frac{h2}{h3}$	1.12 ± 0.05	0.96 ± 0.05	
UGC 6484	part	hg	hz	$\frac{hg}{hz}$
	total	14.2 ± 0.3	13.7 ± 0.1	1.04 ± 0.02
	arms	15.7 ± 0.1	14.8 ± 0.2	1.06 ± 0.02
	interarms	12.9 ± 0.2	13.0 ± 0.2	0.99 ± 0.02
	$\frac{h2}{h3}$	1.21 ± 0.02	1.14 ± 0.02	

Table D.4: scale lengths of the Type 5 galaxies

Appendix E

Least squares fits: plots

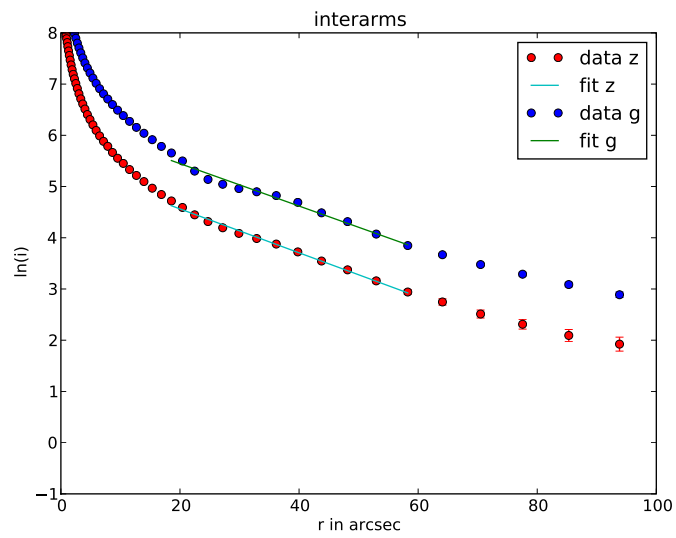
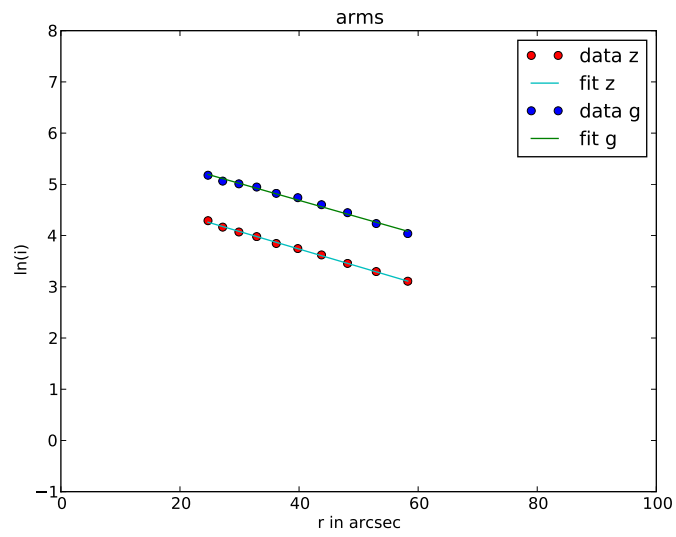
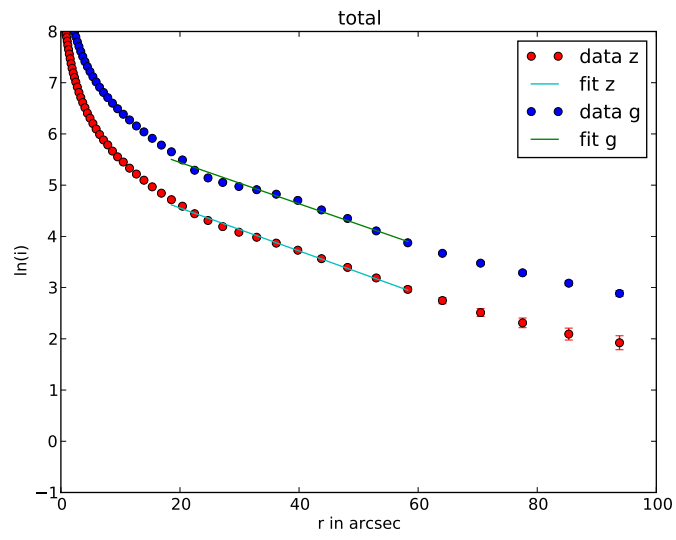


Figure E.1: UGC 4820

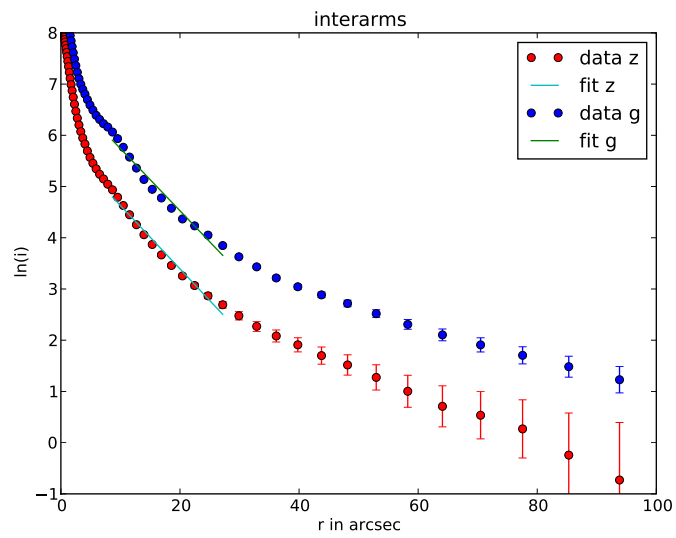
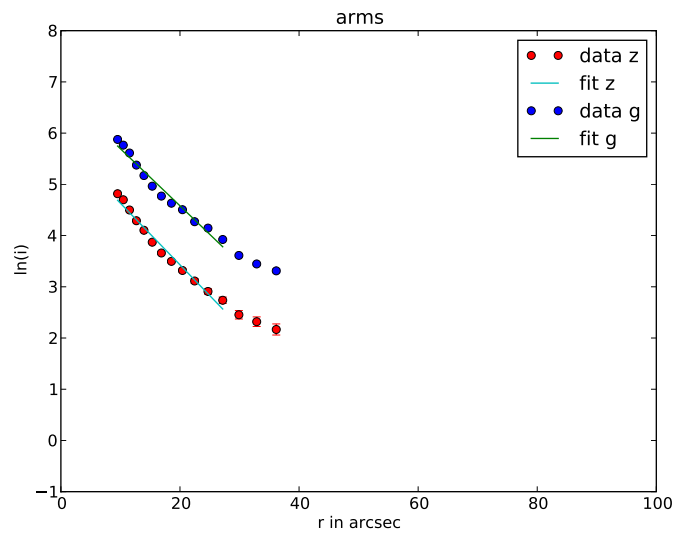
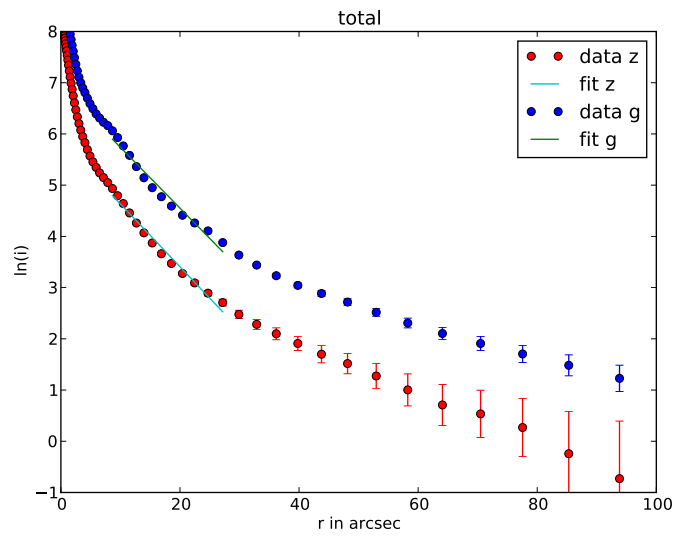


Figure E.2: UGC 5731

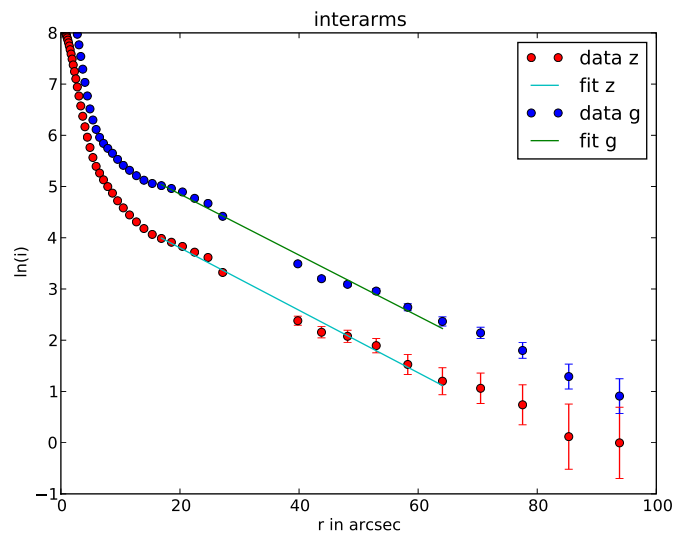
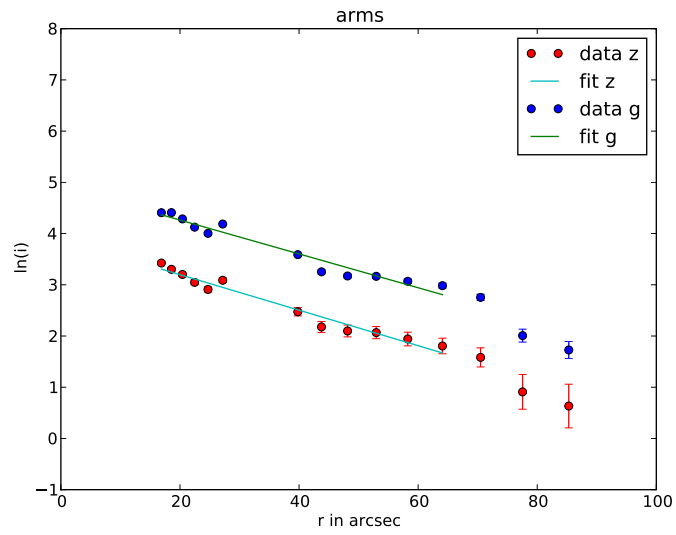
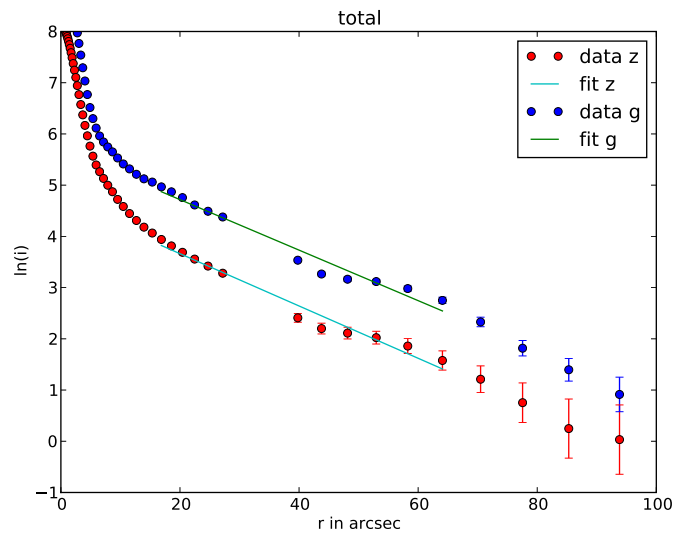


Figure E.3: UGC 6118

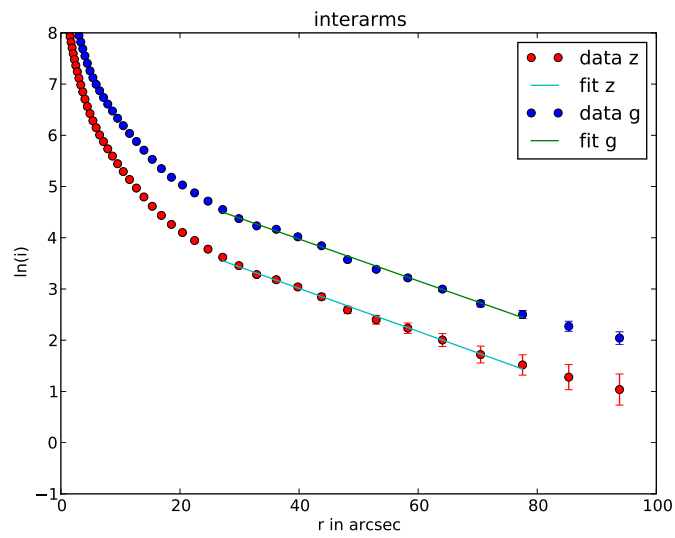
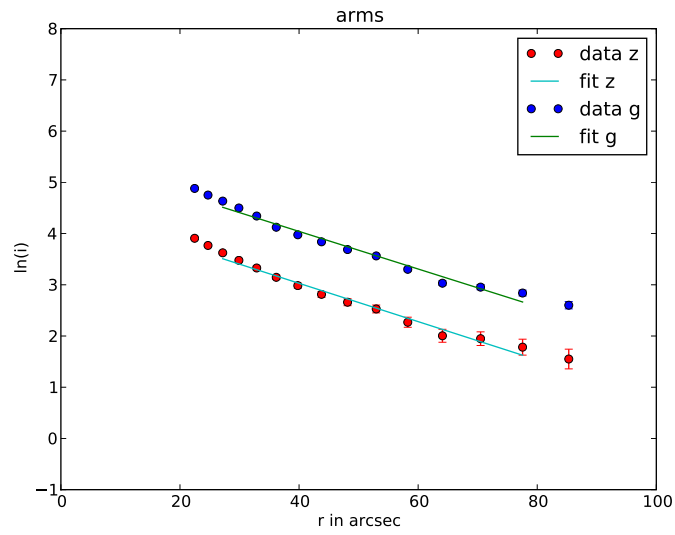
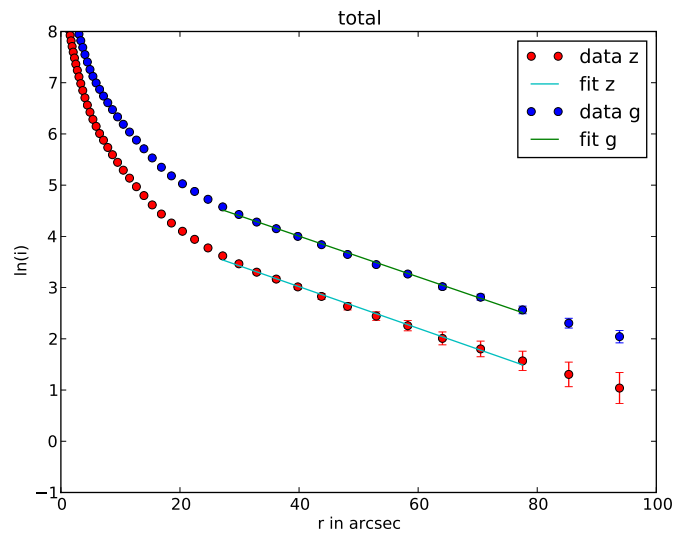


Figure E.4: UGC 6878

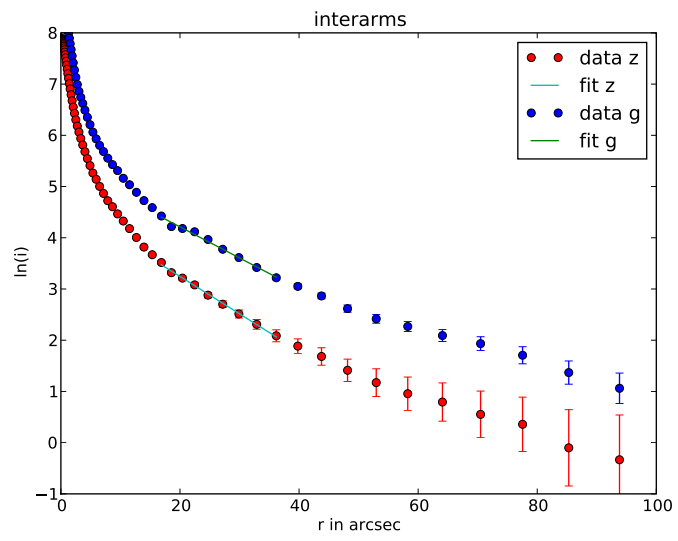
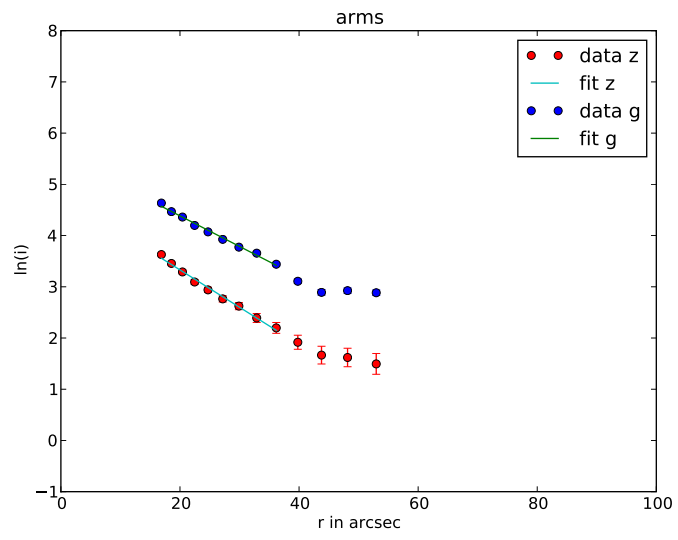
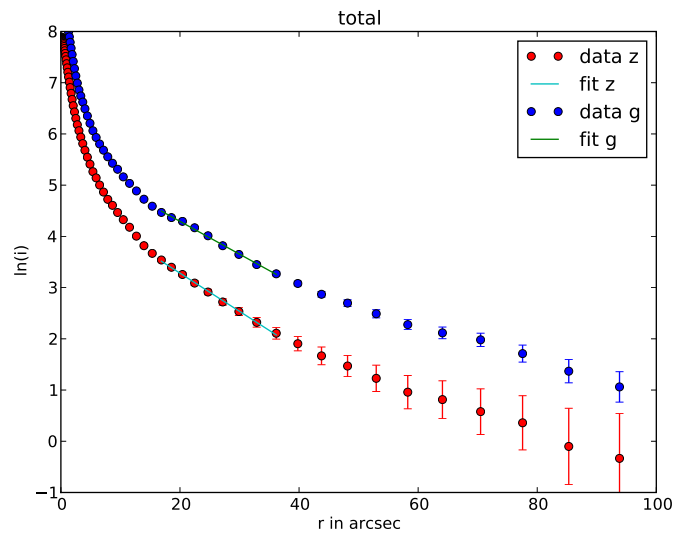


Figure E.5: UGC 9133

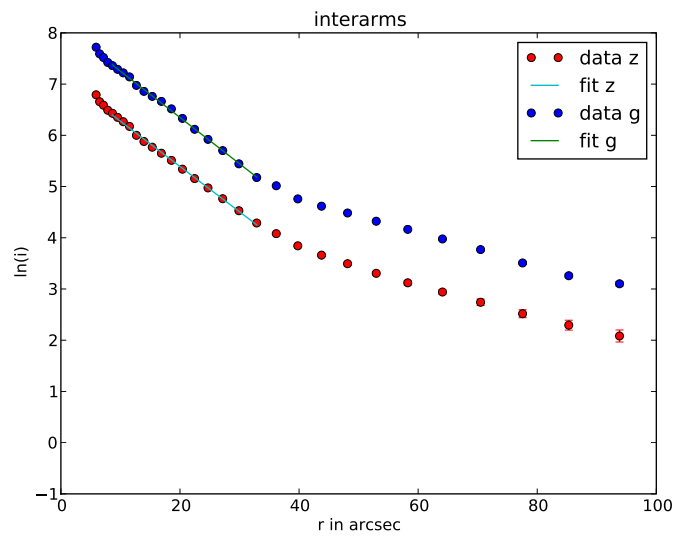
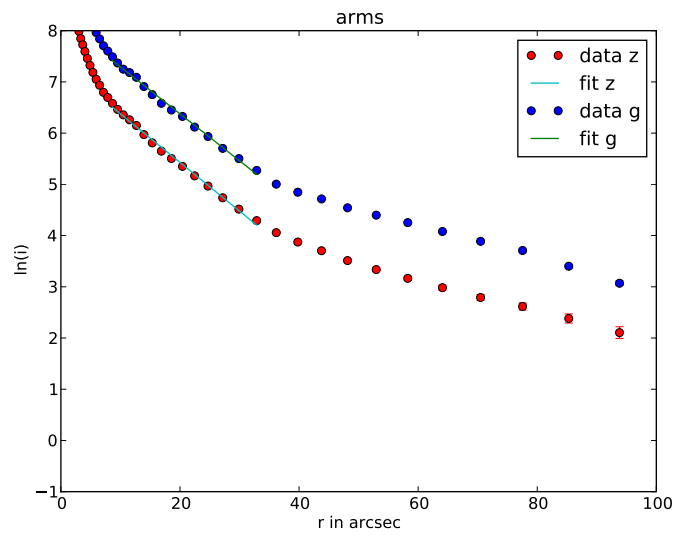
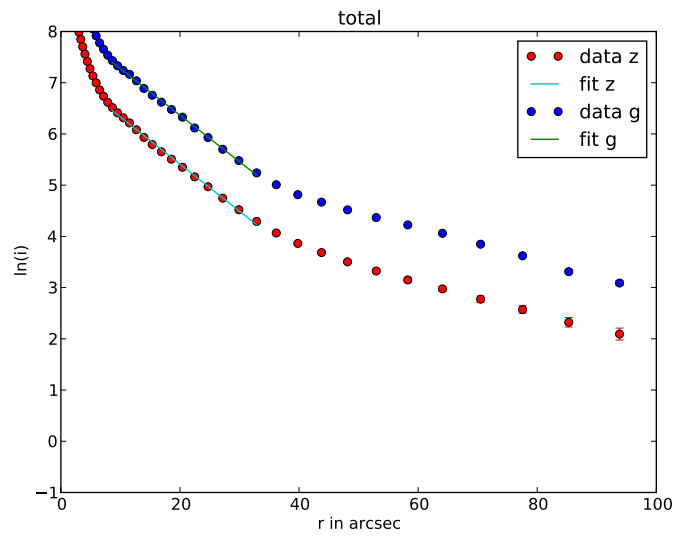


Figure E.6: MCG-1-33-13

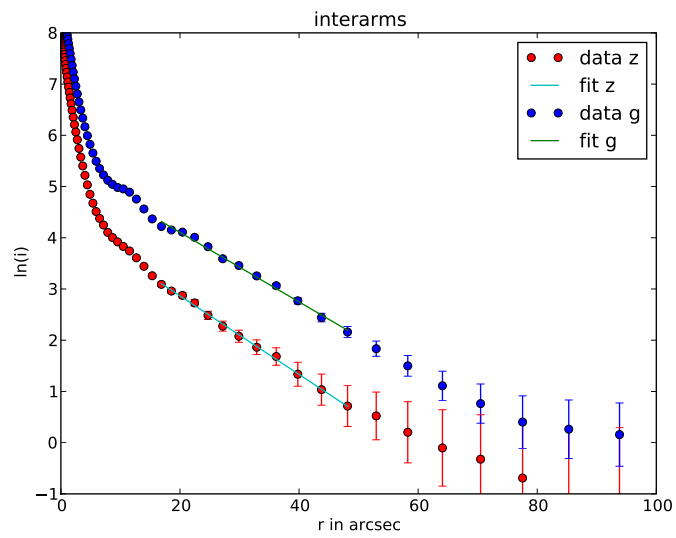
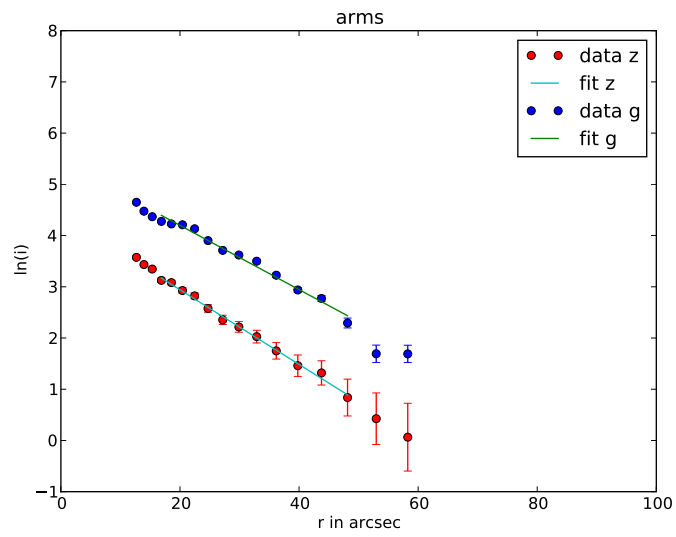
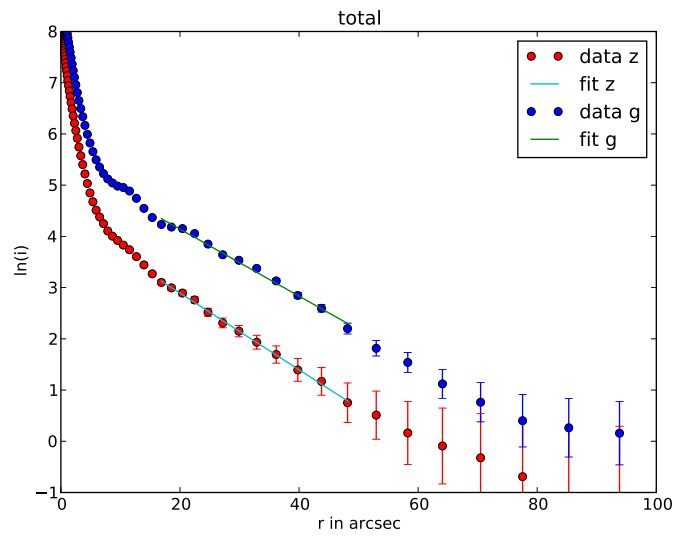


Figure E.7: UGC 12702

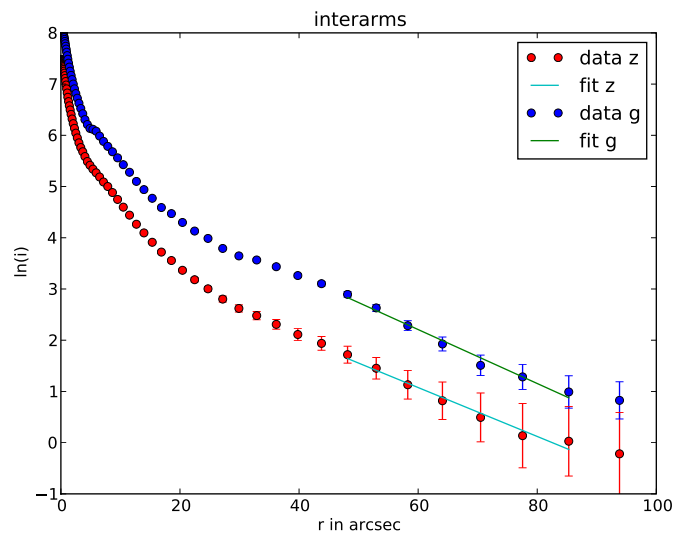
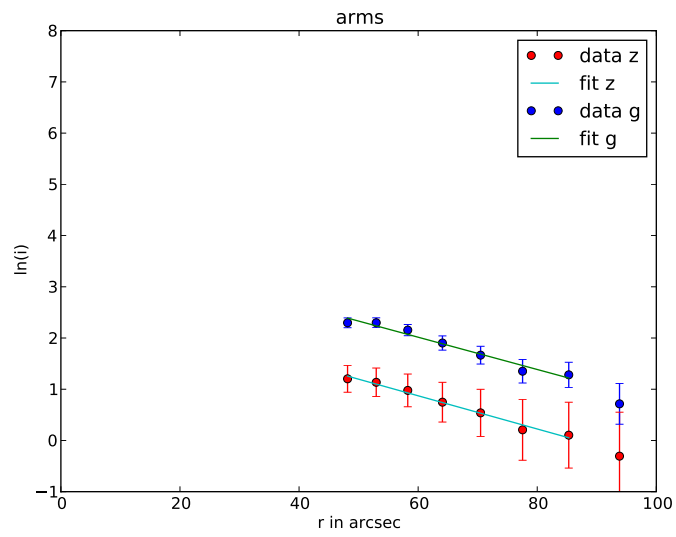
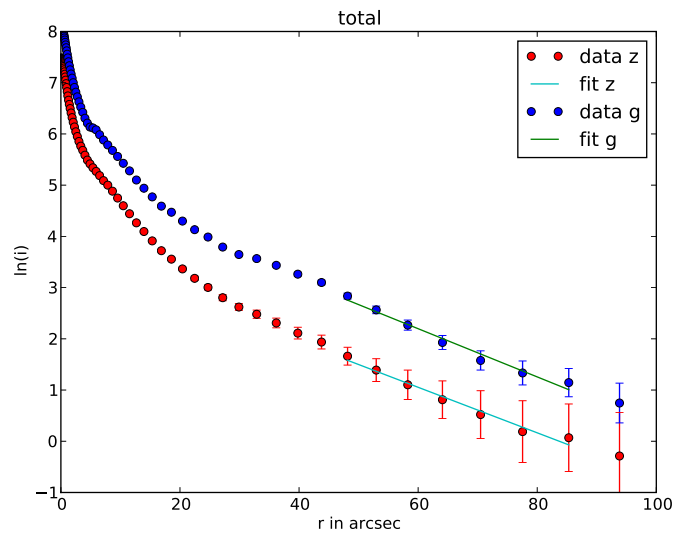


Figure E.8: UGC 2200

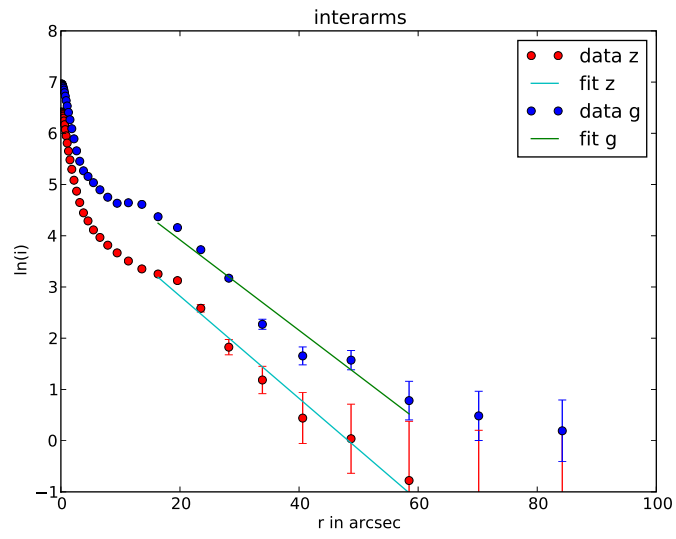
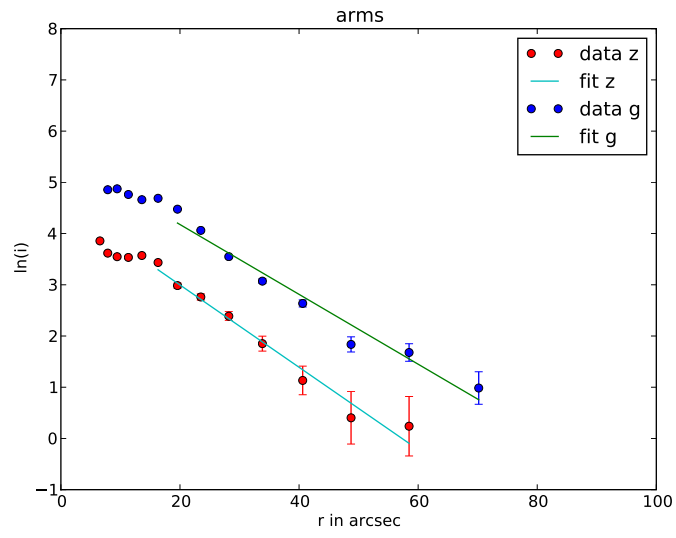
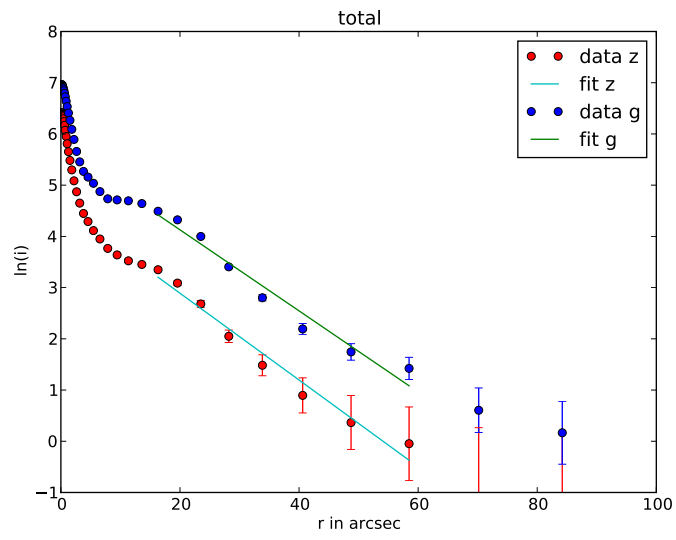


Figure E.9: UGC 7067

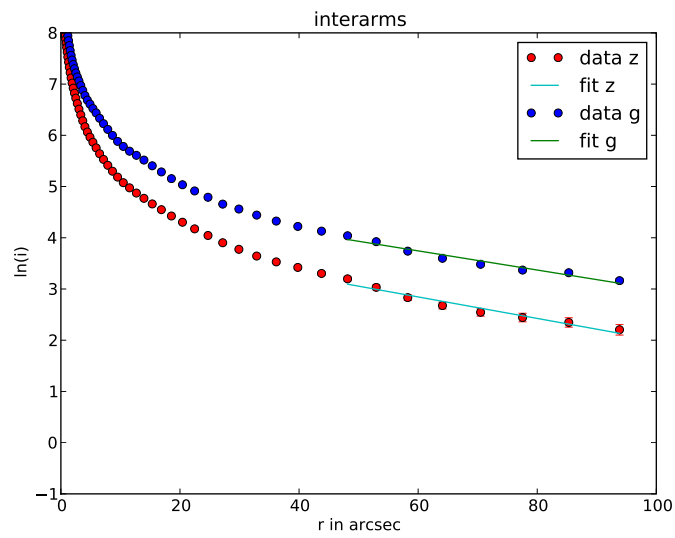
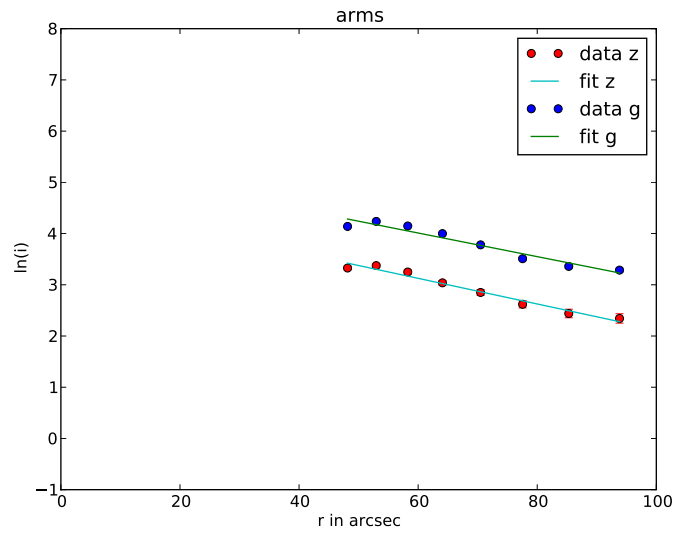
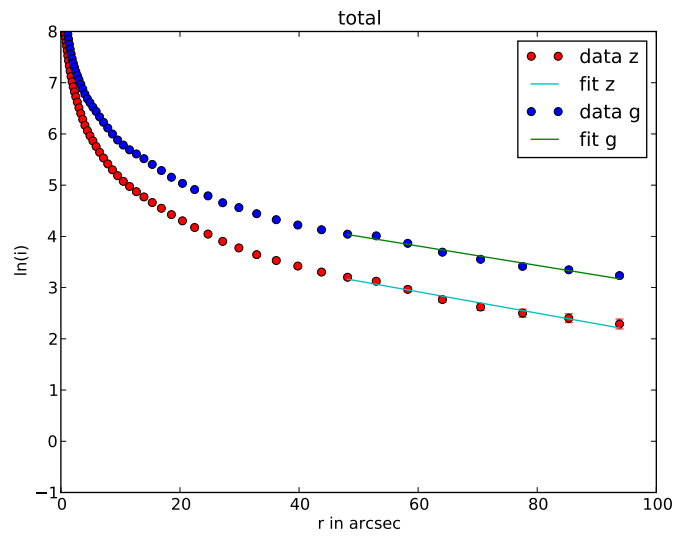


Figure E.10: UGC 7753

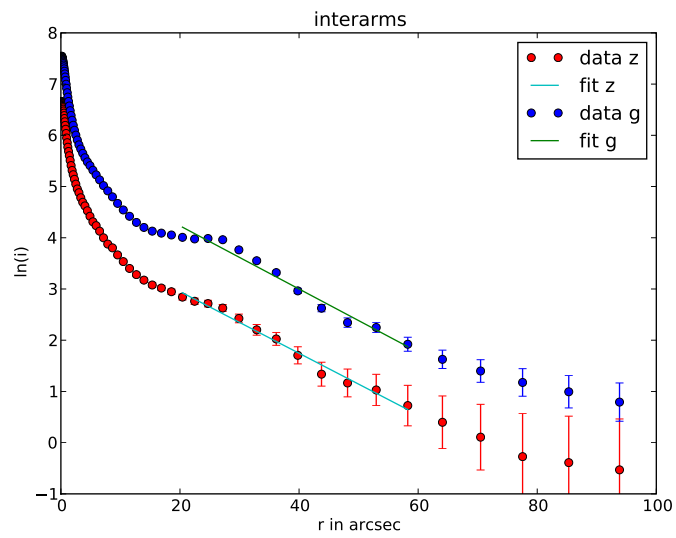
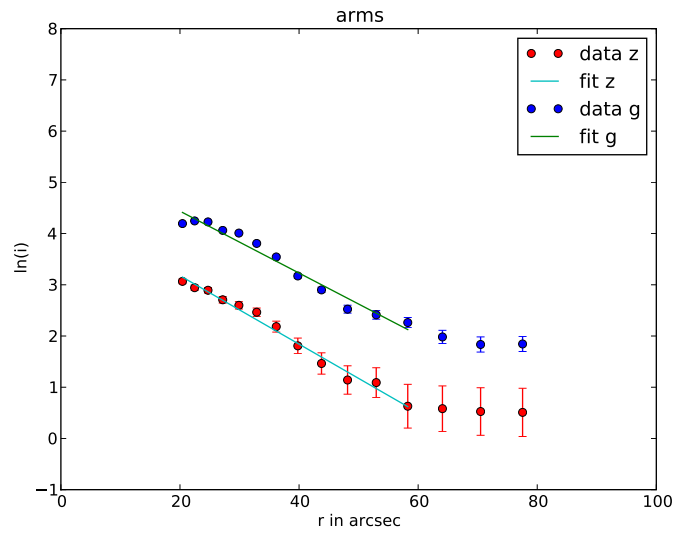
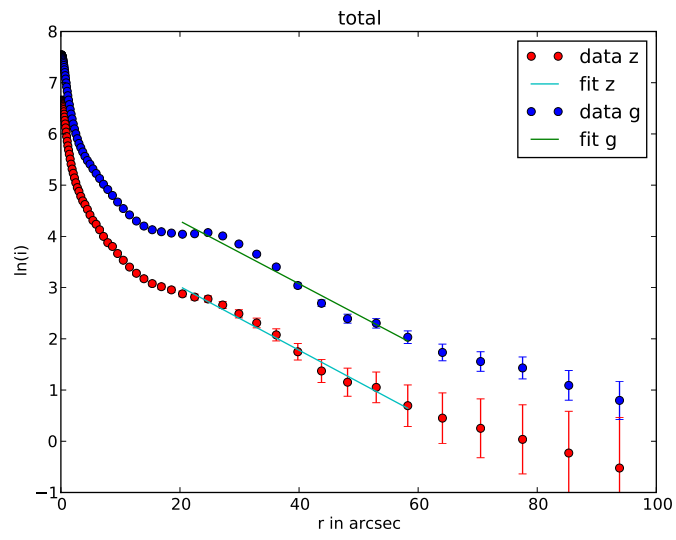


Figure E.11: UGC 9915

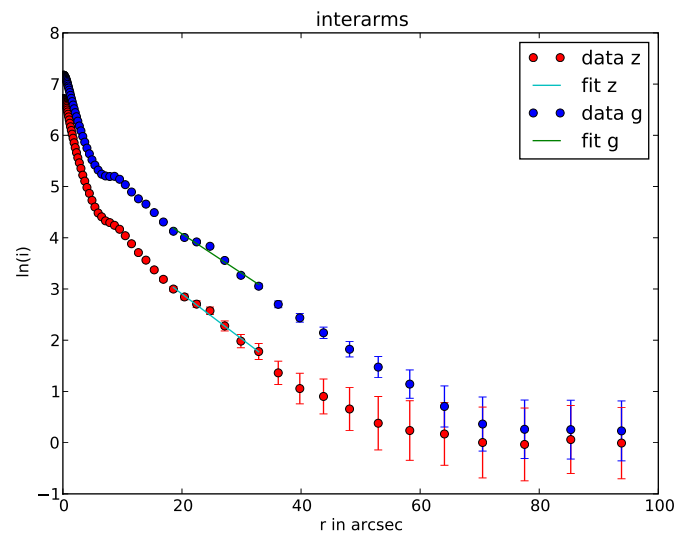
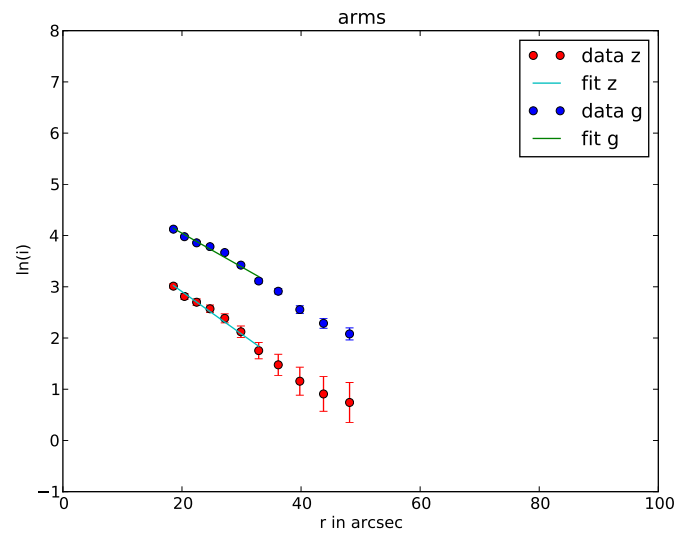
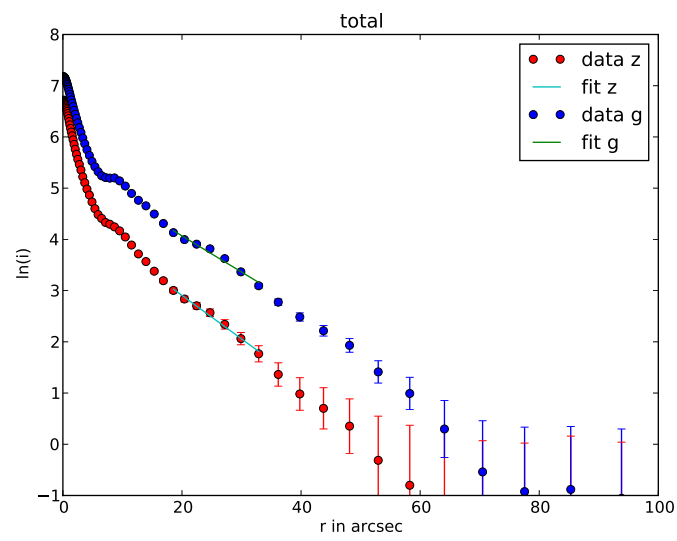


Figure E.12: UGc 4503

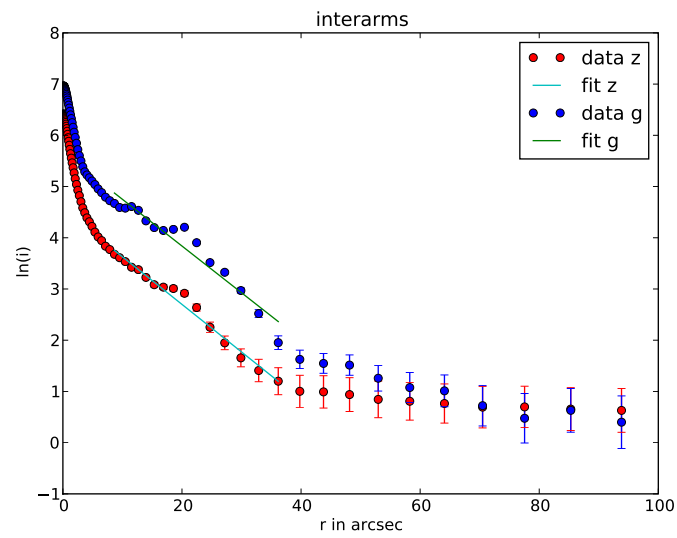
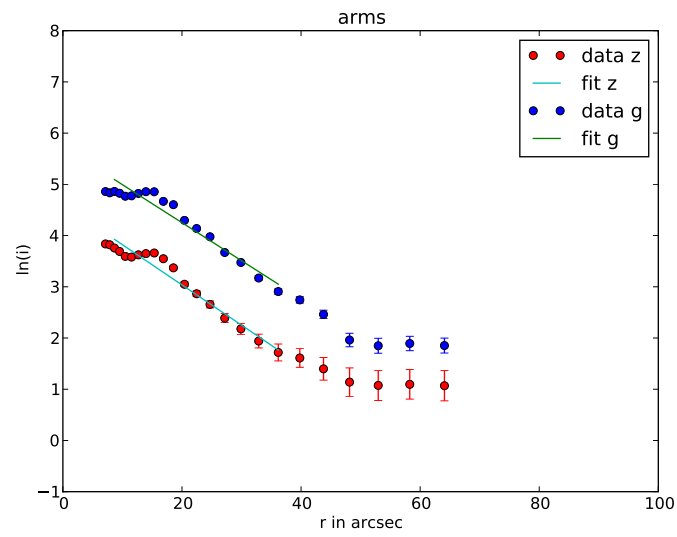
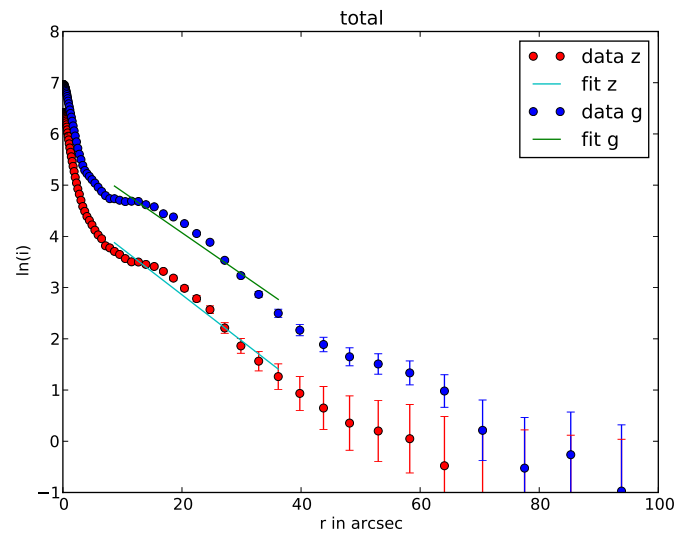


Figure E.13: UGC 7067

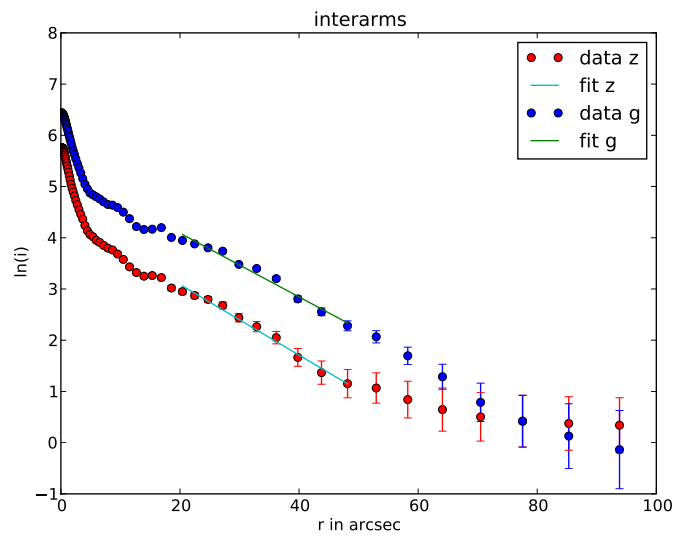
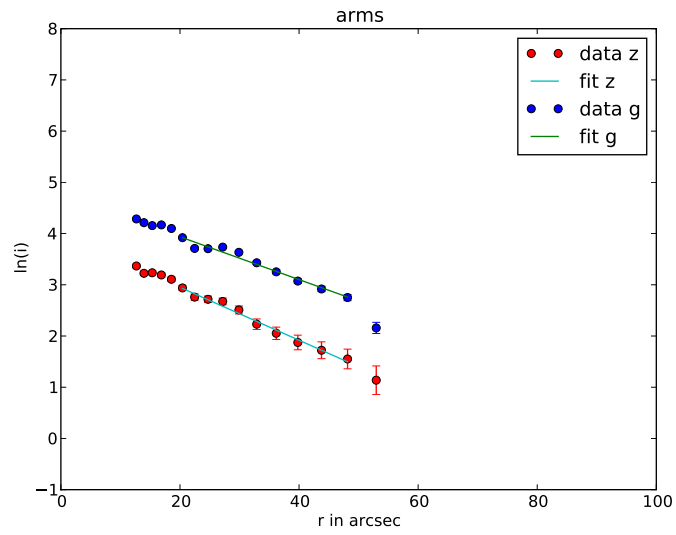
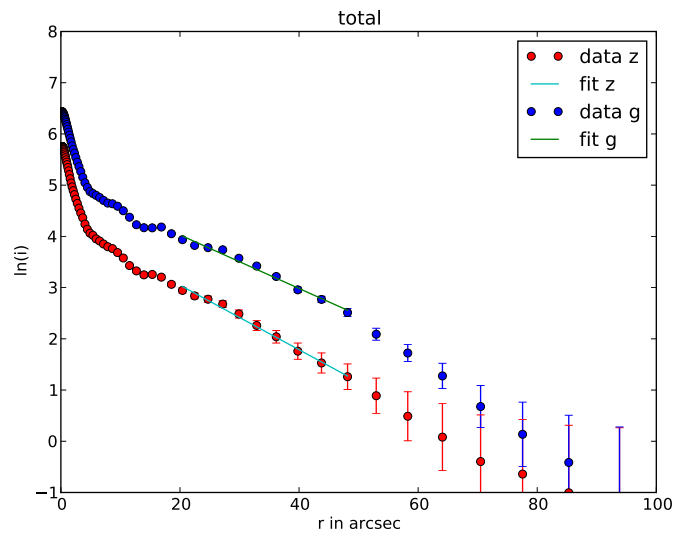


Figure E.14: UGC 7225

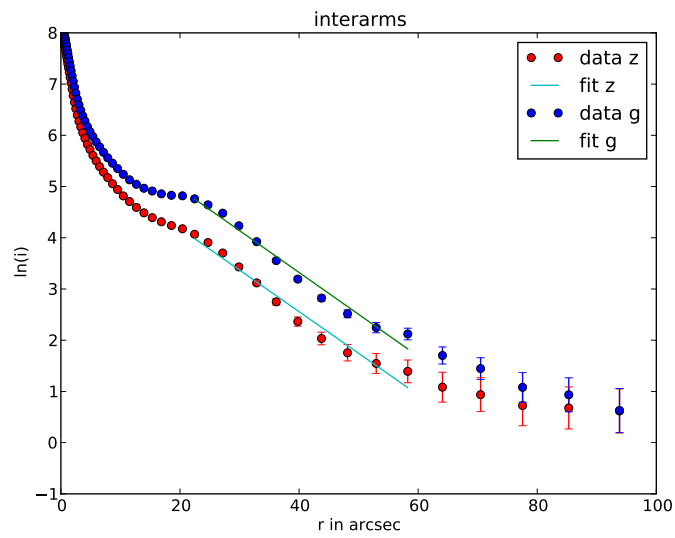
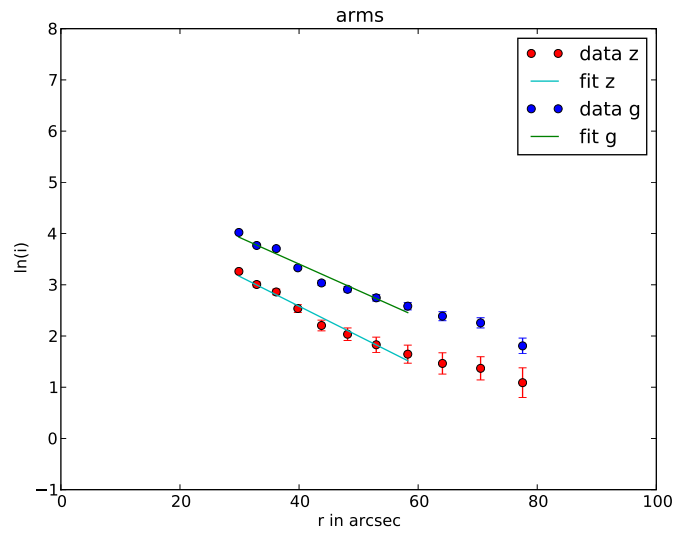
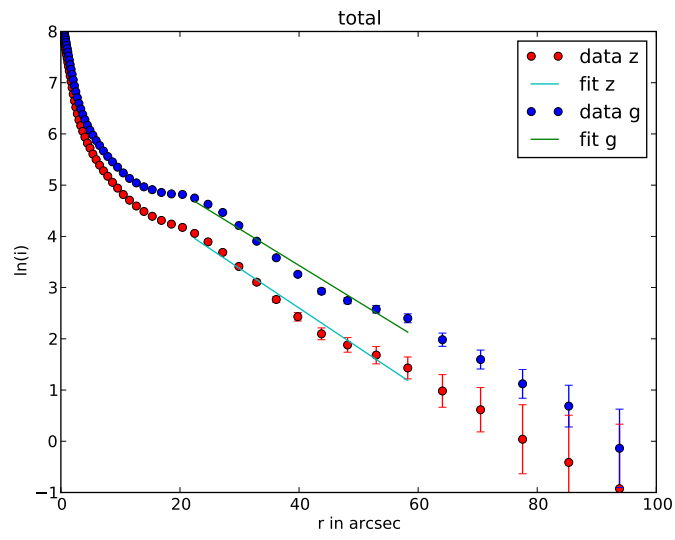


Figure E.15: UGC 7884

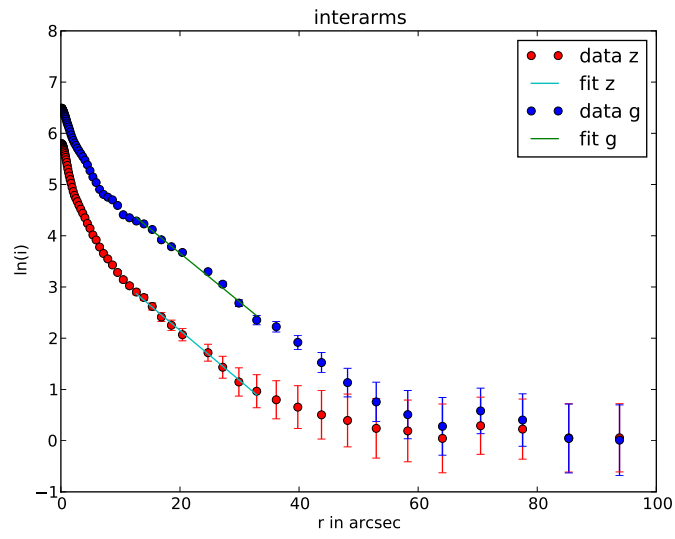
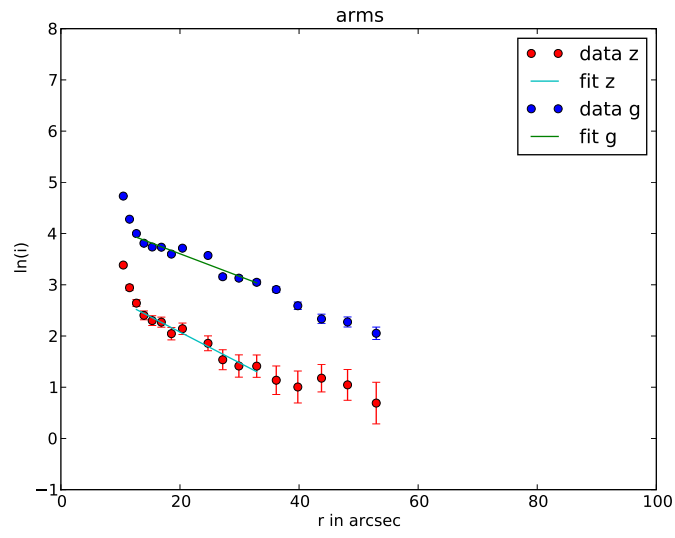
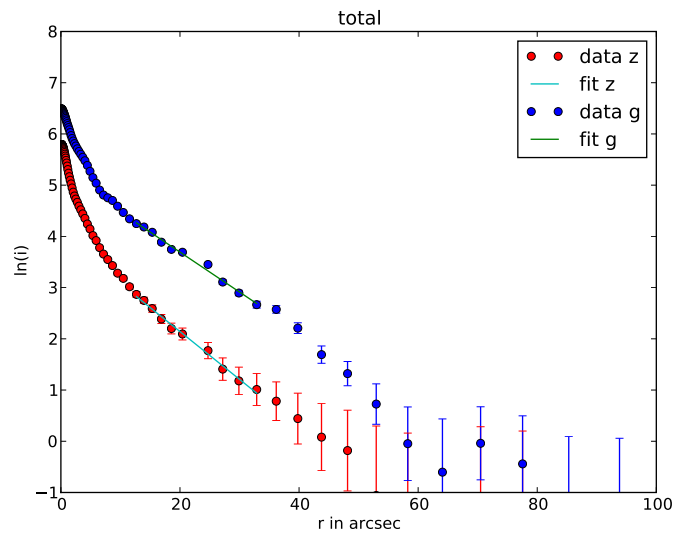


Figure E.16: UGC 9334

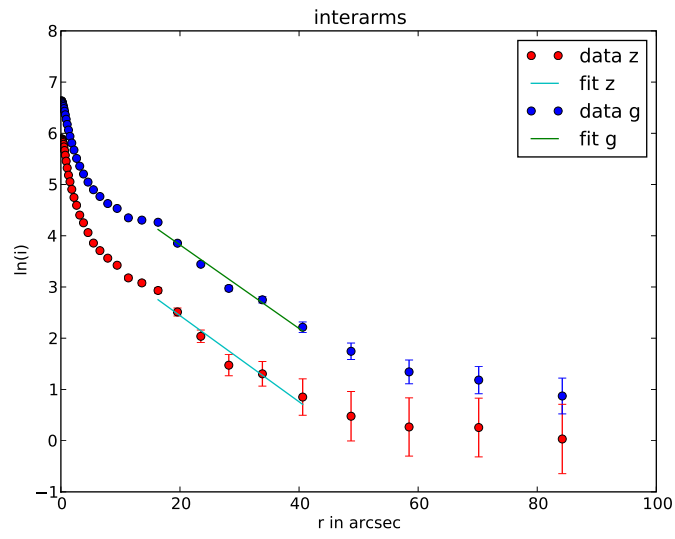
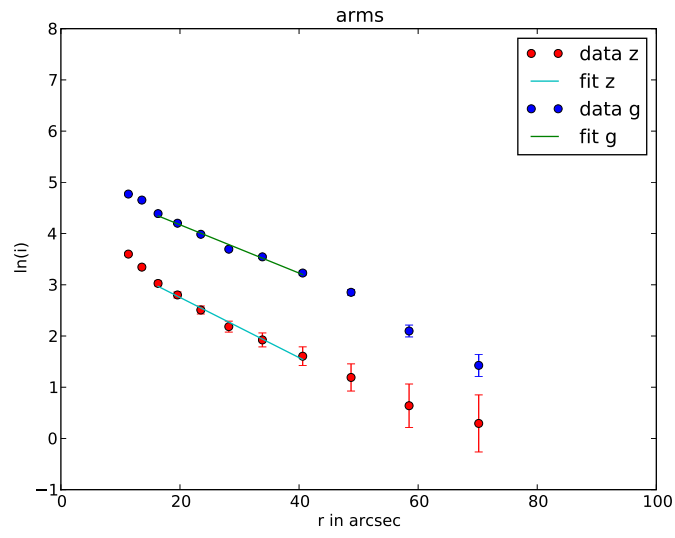
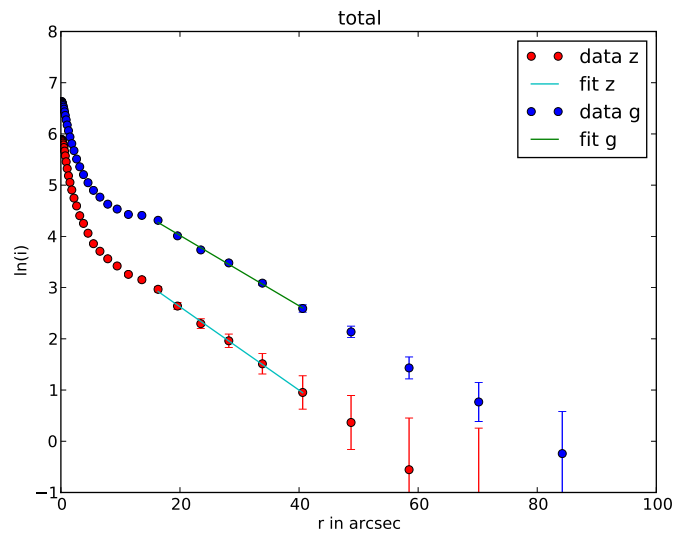


Figure E.17: UGC 9481

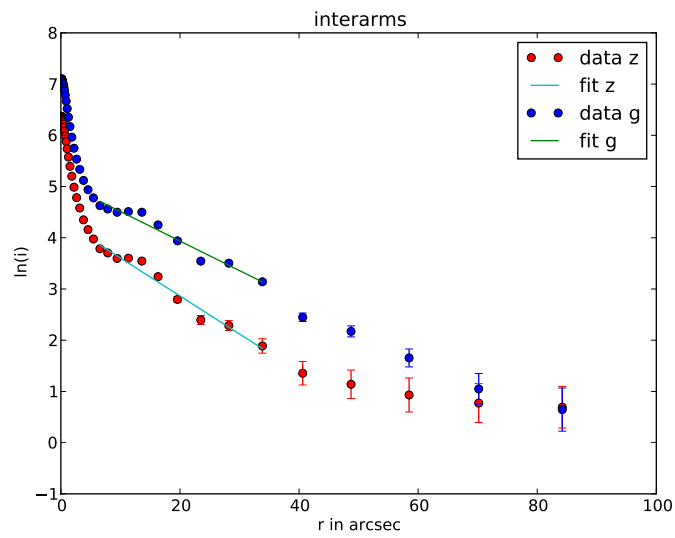
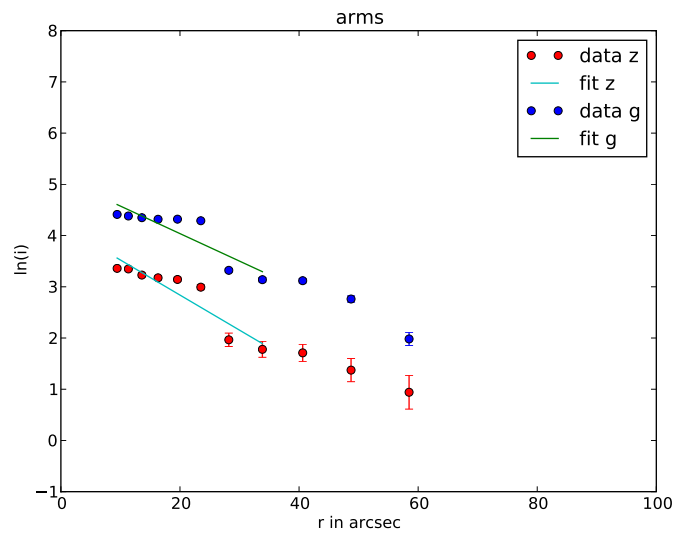
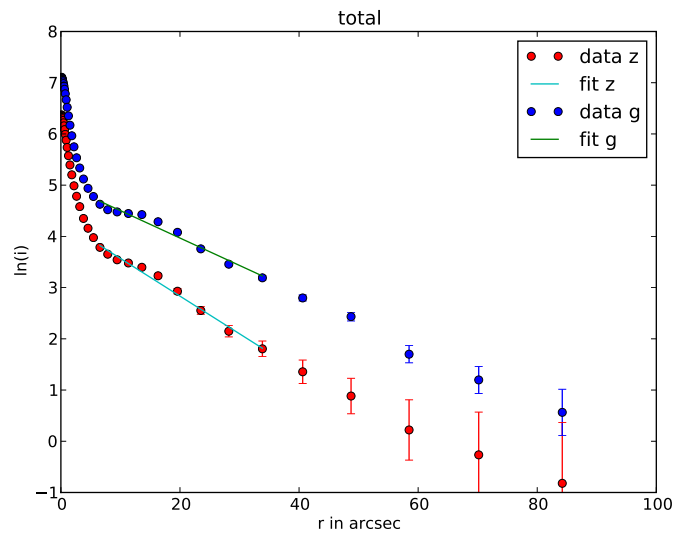


Figure E.18: ESO 569-22

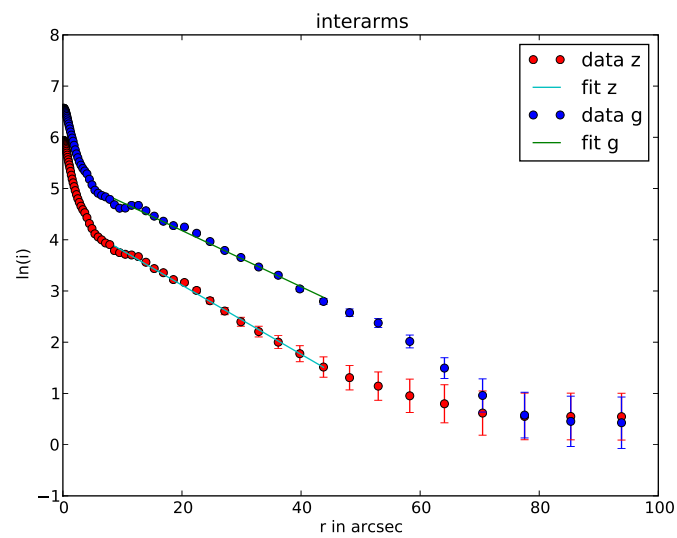
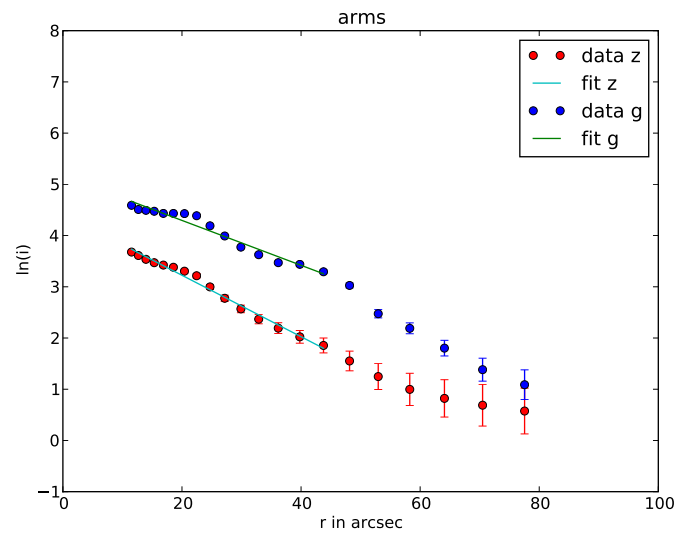
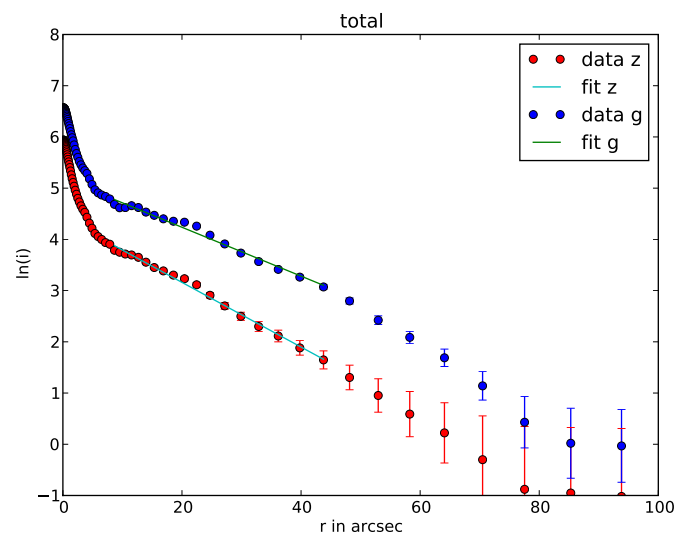


Figure E.19: MCG-1-35-16

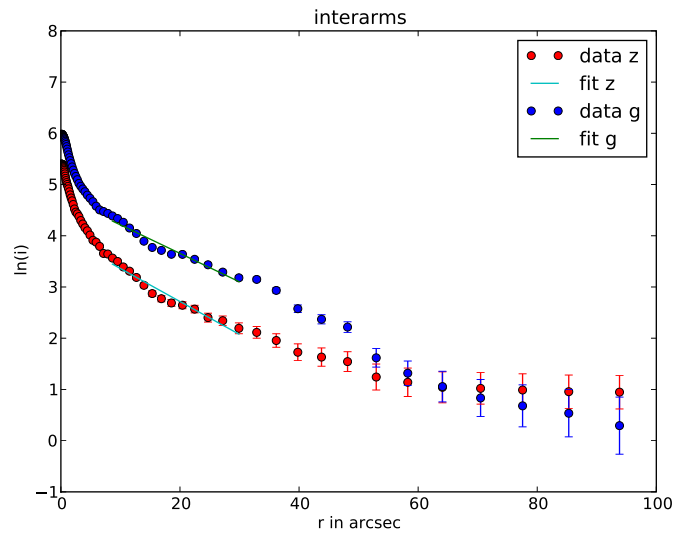
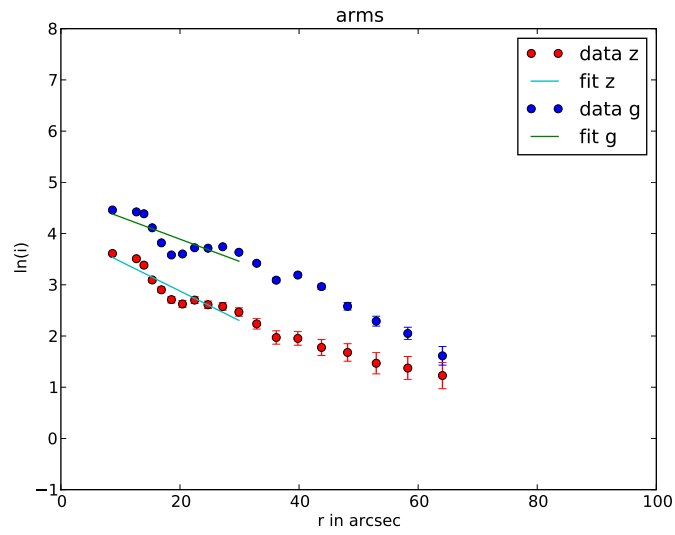
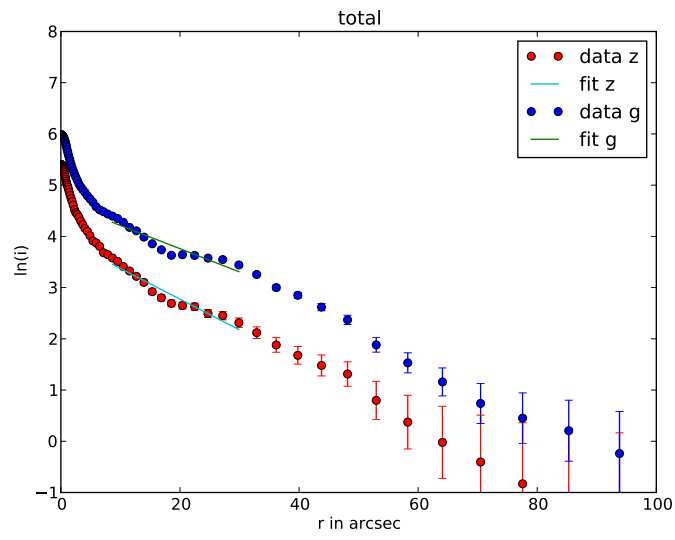


Figure E.20: UGC 12788

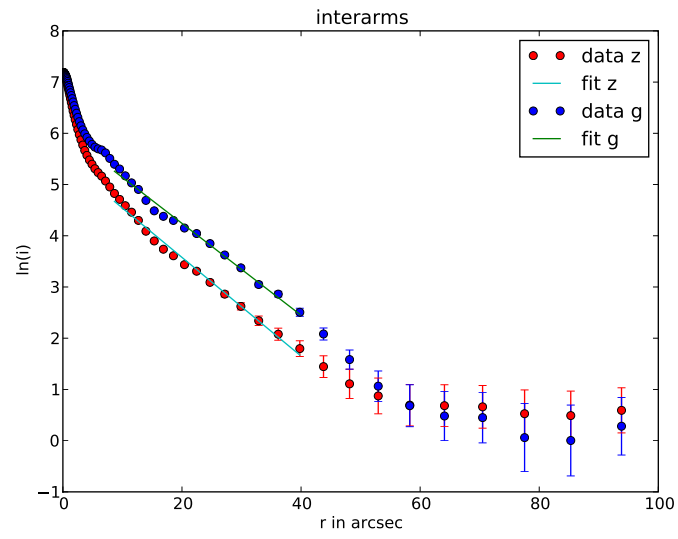
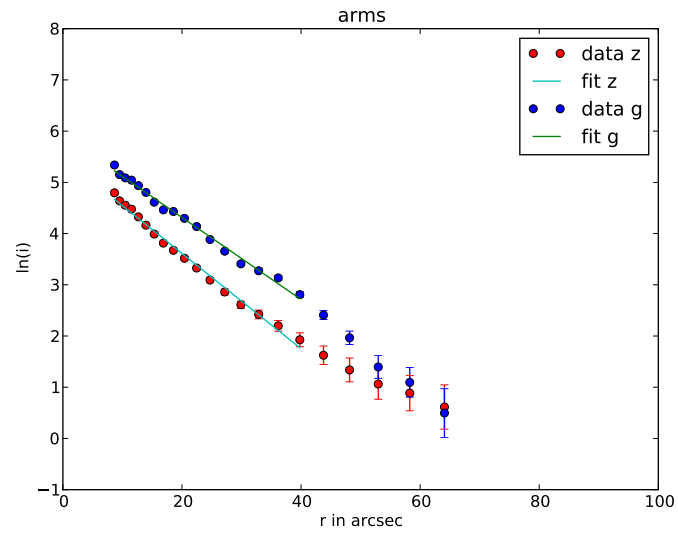
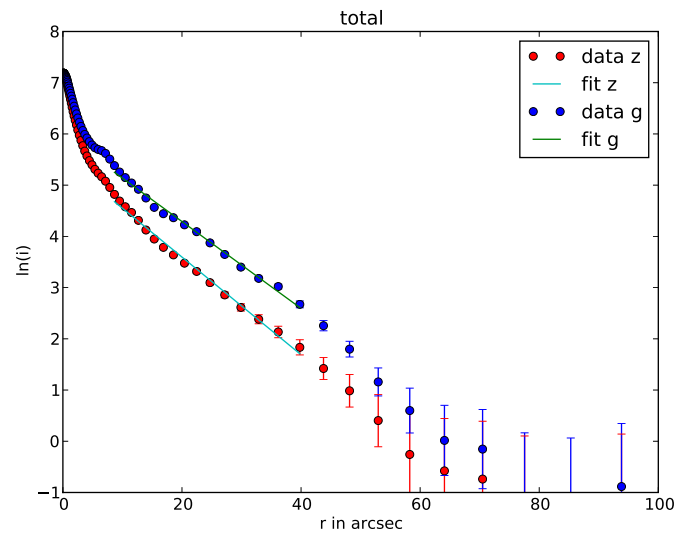


Figure E.21: UGC 438

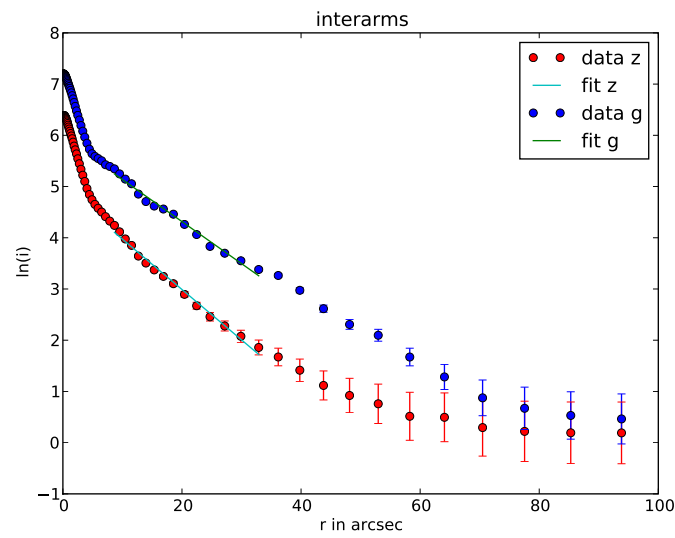
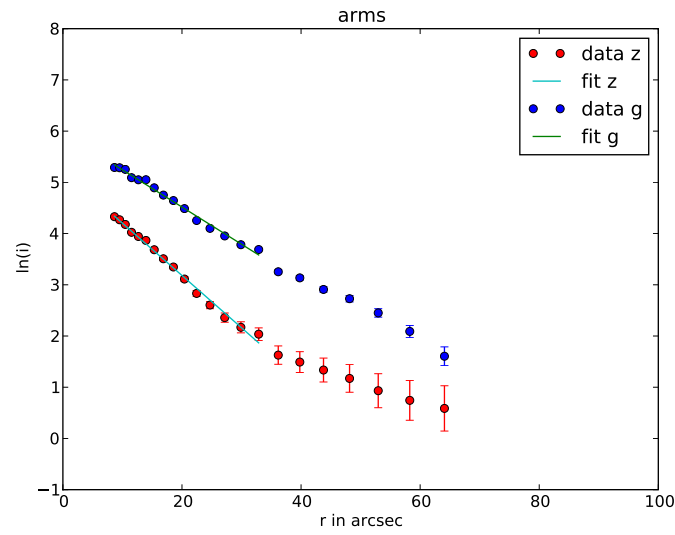
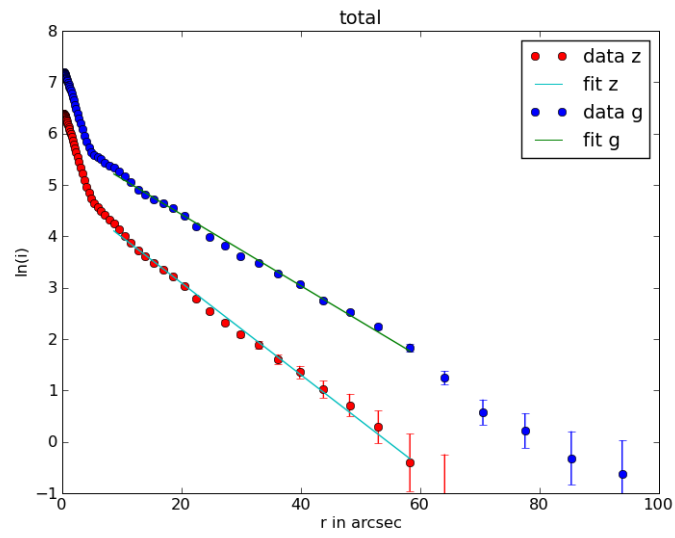


Figure E.22: UGC 5887

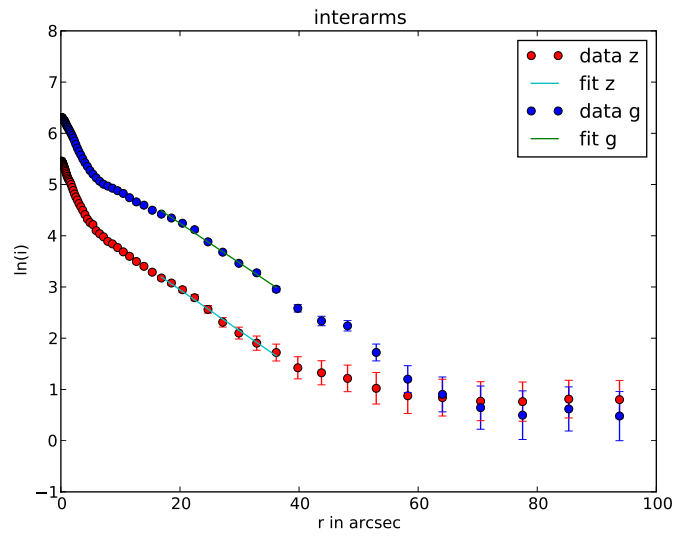
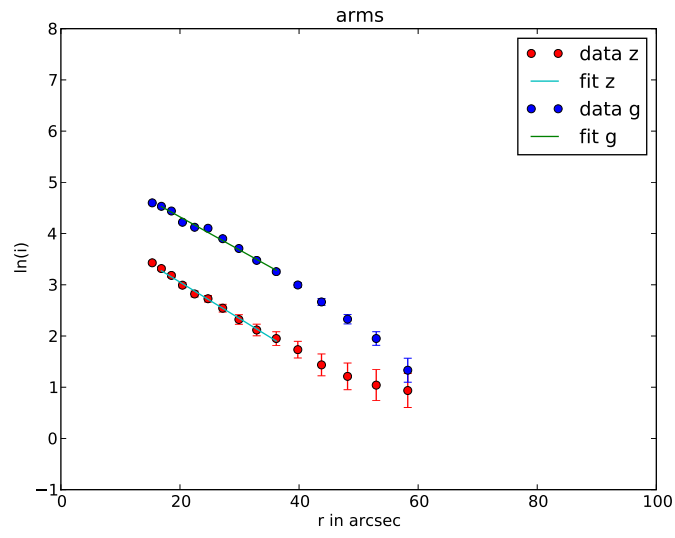
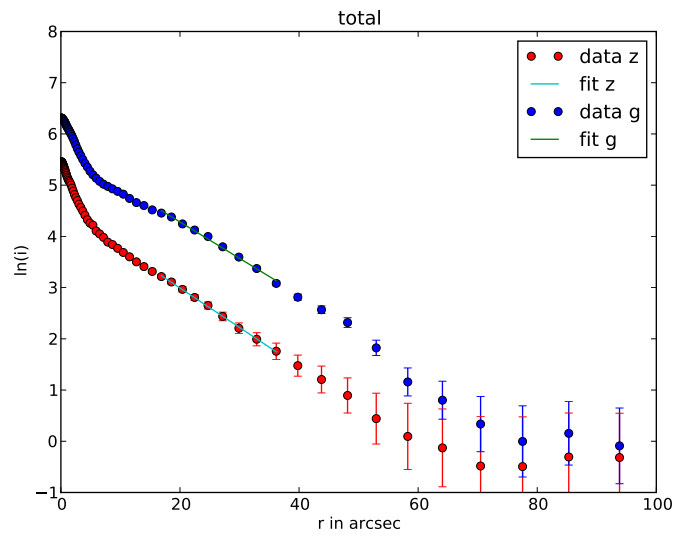


Figure E.23: UGC 6484